NASA TECHNICAL NOTE

NASA TN D-6669
C. /

THE EFFECT OF INJECTION ANGLE ON THE INTERACTION BETWEEN SONIC SECONDARY JETS AND A SUPERSONIC FREE STREAM

by Charles R. McClinton

Langley Research Center

Hampton, Va. 23365

0133461

1. Report No. NASA TN D-6669	2. Government Accession No.	3. Recipient's Catalog No.
4. Title and Subtitle THE EFFECT OF INJECTION ANGLE ON THE INTERACTION BETWEEN SONIC SECONDARY JETS AND A SUPERSONIC FREE STREAM		5. Report Date February 1972
		6. Performing Organization Code
7. Author(s) Charles R. McClinton		8. Performing Organization Report No. L-8125
		10. Work Unit No. 764-75-01-06
9. Performing Organization Name and Address NASA Langley Research Center Hampton, Va. 23365		11. Contract or Grant No.
		13. Type of Report and Period Covered Technical Note
12. Sponsoring Agency Name and Address National Aeronautics and Space Administration Washington, D.C. 20546		14. Sponsoring Agency Code

15. Supplementary Notes The information presented herein was offered as a thesis in partial fulfillment of the requirements for the degree of Master of Science from the School of Engineering and Applied Science, George Washington University, Washington, D.C., February 1971.

16. Abstract

An experimental investigation, as part of a research program on the development of technology for the design of supersonic combustion ramjets, has been conducted to determine the effect of injection angle on the jet penetration, mixing rate, and airstream total-pressure recovery downstream of five laterally spaced sonic hydrogen jets flush mounted on a flat plate. The hydrogen was injected at a ratio of jet dynamic pressure to free-stream dynamic pressure of unity into a Mach 4.04 free stream with a turbulent boundary layer 3.40 injector diameters thick at the injection station. Fuel was injected at angles measured from the plate surface of 30°, 45°, 60°, and 90°, and the flow field was surveyed at 30, 60, and 120 injector diameters downstream to obtain hydrogen concentration, pitot pressure, and static pressure. Results of this investigation indicated that at the lower injection angles less free-stream momentum loss was required to turn and accelerate the injected gas downstream and, thereby, less flow disturbance and total-pressure loss were produced. In addition, the lower injection angles resulted in improved fuel distribution and faster mixing of the injected gas with the free stream. A correlating parameter, developed from considerations of the effective-momentum-flux differences between the injected gas and the free-stream air, predicted greater penetration and faster mixing for the lower injection angles.

17. Key Words (Suggested by Author(s)) Injection angle Supersonic combustor Wall injection Fuel penetration Turbulent mixing	18. Distribution Statement Unclassified — Unlimited		
19. Security Classif. (of this report) Unclassified	20. Security Classif. (of this page) Unclassified	21. No. of Pages 33	22. Price* $3.00

THE EFFECT OF INJECTION ANGLE ON THE INTERACTION BETWEEN
SONIC SECONDARY JETS AND A SUPERSONIC FREE STREAM[*]

By Charles R. McClinton
Langley Research Center

SUMMARY

An experimental investigation, as part of a research program on the development of technology for the design of supersonic combustion ramjets, has been conducted to determine the effect of injection angle on the jet penetration, mixing rate, and airstream total-pressure recovery downstream of five laterally spaced sonic hydrogen jets flush mounted on a flat plate. The hydrogen was injected at a ratio of jet dynamic pressure to free-stream dynamic pressure of unity into a Mach 4.04 free stream with a turbulent boundary layer 3.40 injector diameters thick at the injection station. Fuel was injected at angles measured from the plate surface of 30°, 45°, 60°, and 90°, and the flow field was surveyed at 30, 60, and 120 injector diameters downstream to obtain hydrogen concentration, pitot pressure, and static pressure. Results of this investigation indicated that at the lower injection angles less free-stream momentum loss was required to turn and accelerate the injected gas downstream and, thereby, less flow disturbance and total-pressure loss were produced. In addition, the lower injection angles resulted in increased penetration at the downstream stations surveyed and faster mixing of the injected gas with the free stream. A correlating parameter, developed from considerations of the effective-momentum-flux differences between the injected gas and the free-stream air, predicted greater penetration and faster mixing for the lower injection angles.

INTRODUCTION

The development of concepts for hypersonic air-breathing propulsion systems has created a need for the refinement and optimization of all aspects of the design of the supersonic combustion ramjet (scramjet) engine. The accurate design of the supersonic combustion chamber depends on knowledge of fuel-air mixing characteristics. The primary objectives of the fuel-injector arrangement are to obtain a reasonably uniform

[*]The information presented herein was offered as a thesis in partial fulfillment of the requirements for the degree of Master of Science from the School of Engineering and Applied Science, George Washington University, Washington, D.C., February 1971.

combustible-fuel distribution across the combustion chamber within a short combustor length and to produce a minimal pressure loss in the combustor airstream. In an optimized combustor design it is probable that fuel will be injected from points in the stream (i.e., from struts) as well as from the wall; however, only injection from the wall is considered in the present study.

Historically, interest in the mixing or interaction of a secondary jet with a supersonic mainstream has developed in several fields. A survey of the literature indicates that most scramjet-oriented studies have been performed using a single, underexpanded jet issuing normal to the air flow; the analysis was aimed primarily at jet penetration and at the shock-wave structure in proximity to the injector (refs. 1 to 5). This type of analysis has proved useful in the preliminary design of ramjet fuel-injection systems, but system optimization also requires a knowledge of the downstream mixing region. Some work has been presented in the literature which considers both the initial interaction effects and the downstream aspects of the mixing problem. Much of the downstream analysis results from schlieren data (refs. 6 to 10) which are limited to penetration correlations for air flow with relatively thin boundary layers. Other analyses are based on results from surveys of pitot pressure and injected-gas concentration in the downstream mixing region. This survey procedure produces fuel-distribution contours which are used in determining mixing rates, in addition to defining penetration. Several studies (refs. 11 to 18) have evaluated the effect of different flow (jet and free-stream) variables on the jet penetration and mixing rate. However, studies on the effect of injection angle, references 6, 7, and 15, have produced only limited results. The data from references 6 and 7 pertain to measurements in the immediate vicinity of the jet. These measurements are not representative of the ramjet problem of fuel distribution and mixing in the downstream region where the fuel-air mixture approaches a stoichiometric ratio. On the other hand, the results from reference 15, although measured in the downstream region, were obtained in a confined cylindrical duct; consequently the interpretation of the results is uncertain.

The objective of the present research is to study in some detail the effect of secondary-jet injection angle in an unreacting mixing situation. In the present investigation, values of the following parameters were used which are believed to be representative of scramjet design:

	Value
Ratio of jet dynamic pressure to free-stream dynamic pressure	1.0
Ratio of boundary-layer thickness to jet diameter	3.0
Ratio of jet molecular weight to free-stream molecular weight	0.0691
Jet lateral center-to-center spacing	6.25
Jet Mach number	1.0

The investigation was performed in a Mach 4.04 airstream with secondary injection of hydrogen from a flat-plate model. The tunnel was operated at stagnation pressure of 1.38 MN/m^2, Reynolds number of 6.19×10^7 per meter, and stagnation temperature of approximately 300 K.

SYMBOLS

b	profile shape index (eq. (1))
D	jet diameter, cm
h_{mid}	vertical height to center (middle) of jet Mach disk, cm (fig. 10)
h_{top}	vertical height to upper (top) edge of jet Mach disk, cm (fig. 10)
M	Mach number
$\dot{m}_a$	air flow rate per unit area, $\rho_x u_x (1 - \alpha)$, kg/m^2-s
$\dot{m}_{H_2}$	hydrogen flow rate per unit area, $\rho_x u_x \alpha$, kg/m^2-s
P	jet penetration measured by highest point on contour $\nu = 0.005$, cm (fig. 10)
p	pressure, N/m^2
p_r	pressure recovery, ratio of the mass average total pressure in the mixing region to the mass average total pressure in the undisturbed-airstream tube that feeds the mixing region (fig. 8)
q	dynamic pressure, N/m^2
q_j/q_∞	ratio of jet dynamic pressure to free-stream dynamic pressure
$\left(q_j/q_\infty\right)_{eff}$	effective-dynamic-pressure ratio defined in equation (6)
R_e	Reynolds number
R_x	Reynolds number based on distance from plate leading edge and conditions at edge of boundary layer

u	velocity, m/s
x	axial coordinate, measured downstream from center of middle jet (see fig. 1), cm
y	lateral coordinate, measured across plate from middle jet (see fig. 1), cm
z	vertical coordinate, measured up from middle jet (see fig. 1), cm
α	hydrogen mass fraction
δ	boundary-layer thickness, cm
δ^*	boundary-layer displacement thickness, cm
θ	injection angle, measured from horizontal, deg
θ_B	boundary-layer momentum thickness (fig. 4), cm
ν	hydrogen volume fraction
ρ	density, kg/m^3

Subscripts:

a	air
H_2	hydrogen
j	secondary-jet condition
max	maximum value in mixing region
o	point on vertical survey where $\nu = 0$
ref	point on vertical survey of maximum hydrogen concentration
t	stagnation condition
u	undisturbed plate flow

4

x condition at survey point

α_{max} condition at or location of maximum hydrogen mass fraction

δ condition at boundary-layer edge

∞ free-stream condition

A bar over a symbol denotes a mass averaged value.

APPARATUS AND PROCEDURES

Wind Tunnel and Model

The investigation was conducted using a flat-plate model, shown in figure 1, that spanned a 0.229-meter by 0.229-meter continuous-flow Mach 4.05 tunnel. The plate was 22.87 cm wide and 76.2 cm long; the plate had a replaceable leading edge cut at 10° on the bottom surface with the tip sharpened to 2^O; and the plate was bored and counterbored to form a jet settling chamber and accept a replaceable secondary-jet nozzle block (see settling-chamber detail).
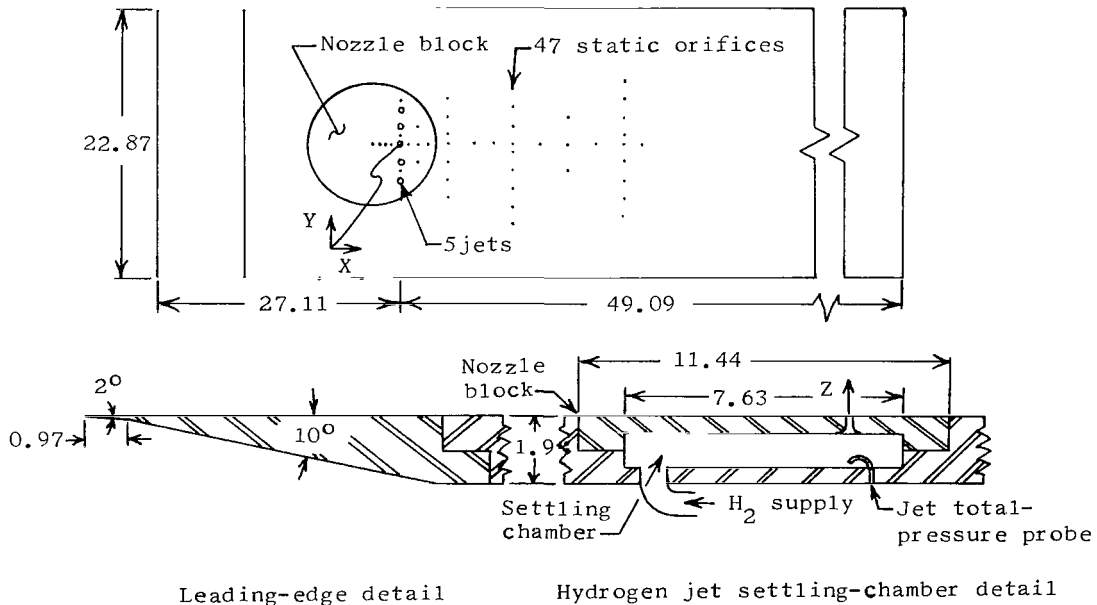
Figure 1.- Sketch of model. (All dimensions in cm.)

Individual nozzle blocks were fabricated for each injection angle with five 0.102-cm-exit-diameter injector nozzles, as illustrated in figure 2, laterally spaced at 0.635 cm. Each of the injector nozzles had a constant area section that was $2\frac{1}{2}$ nozzle exit diameters long. The injector nozzles had measured discharge coefficients of 0.76, 0.83, 0.77, and 0.81 for the 30°, 45°, 60°, and 90° injectors, respectively.
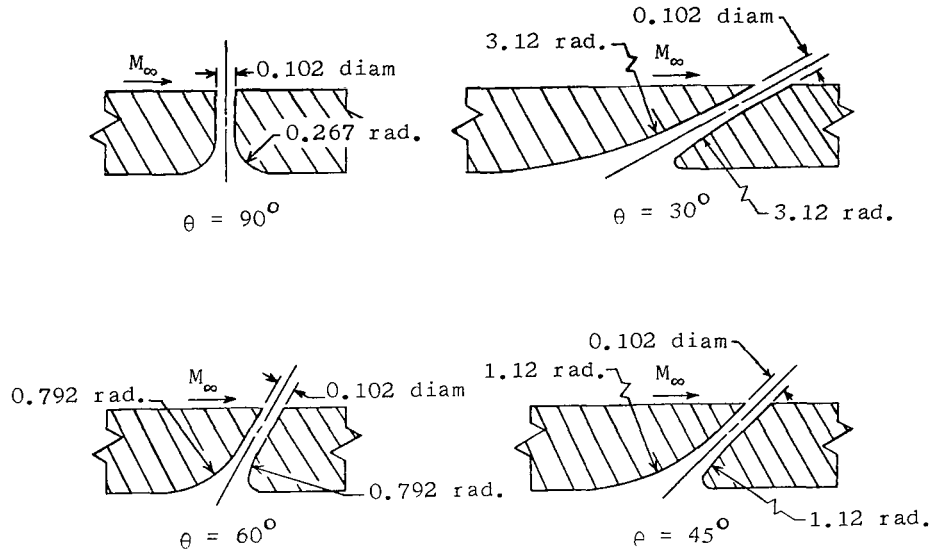

Figure 2.- Details of secondary-jet nozzle. (All dimensions in cm.)

Instrumentation

Instrumentation was provided to measure hydrogen and air stagnation pressures and temperatures, plate-surface static pressures, and in-stream surveys of pitot and static pressures and hydrogen concentration. In addition, the hydrogen mass flow rate was measured using a sharp-edge orifice meter.

Plate static-pressure orifices of 0.051-cm diameter were located on the longitudinal center line from 30 injector diameters ahead of the injector station to 150 injector diameters downstream. In addition, several lateral rows of pressure orifices were located at and downstream of the injection station (see fig. 1). Although data were taken at each orifice, only results on the plate center line and between the jets are presented herein.

The in-stream measurements were made using the probe rake illustrated in figure 3. Spacing between the pitot probe and the static probe was large (3.66 cm) to assure that the static probe did not interfere with pitot-probe readings.

Gas samples were taken from the mixing region by the pitot probe and were analyzed with an on-line process gas chromatograph having a cycle time of 60 seconds. The chromatograph measured only the hydrogen volume fraction and was connected by a series of electrically actuated valves to both the pilot probe and the hydrogen-settling-chamber probe.
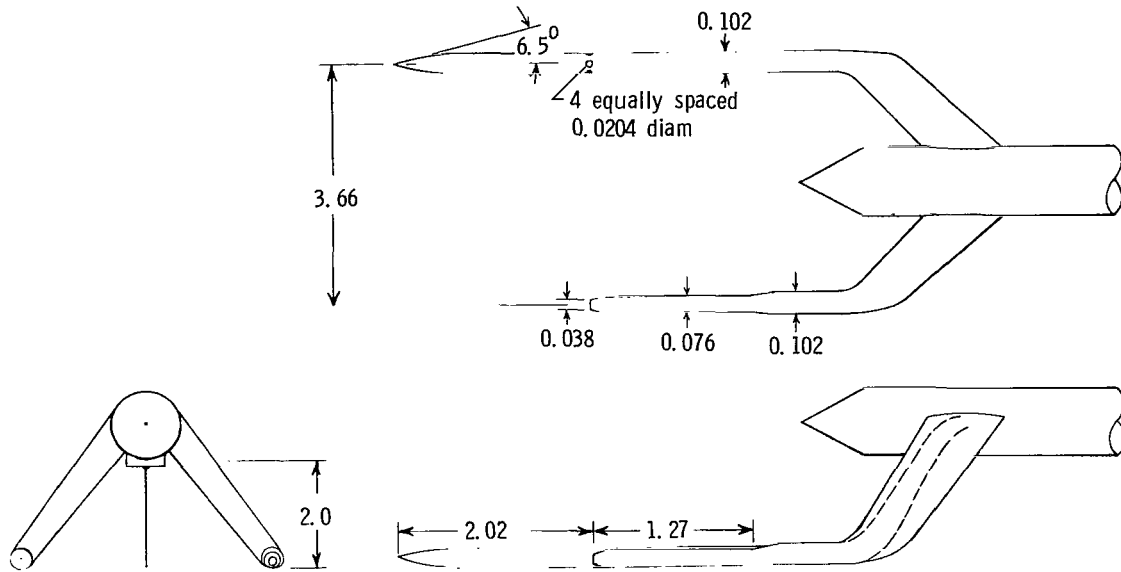
6

Figure 3.- Sketch of pitot- and static-probe rake. (All dimensions in cm.)

Test Conditions and Procedures

The tunnel was operated at a free-stream Mach number of 4.05, at a stagnation pressure of 1.38 MN/m^2, and at a stagnation temperature of approximately 300 K. Reynolds number was 6.19×10^7 per meter. The jet stagnation pressure was 0.28 MN/m^2, which corresponds to q_j/q_∞ of unity. Generally, the jet stagnation temperature was 5 K to 10 K lower than the free-stream stagnation temperature. The hydrogen-air mixing regions were surveyed to obtain pitot pressure, static pressure, and volumetric hydrogen concentration at locations 30, 60, and 120 injector diameters downstream of the injector station. At each station one vertical survey and three horizontal surveys were made. The vertical survey was located directly downstream from the middle-jet center line and extended from the plate surface up to the point of zero hydrogen concentration. The vertical position of the horizontal surveys corresponded to the following three points on the vertical survey: the point of maximum concentration $\left(\alpha_{ref}\right)$, the point halfway between plate and point of maximum concentration, and the point of half-maximum concentration above α_{ref}. All surveys completely spanned the five-jet mixing region.

EXPERIMENTAL RESULTS AND DISCUSSION

Undisturbed Plate Flow

The boundary-layer velocity distribution measured at the jet station with no injection is given in figure 4. The data were reduced assuming a modified Crocco-type temperature velocity profile (ref. 19). The boundary layer was turbulent with a profile

index N of 6.6 $\left(\text{where N is defined by } \dfrac{u}{u_\infty} = \left(\dfrac{z}{\delta}\right)^{1/N}\right)$; the thickness, which is based on

99 percent of the free-stream velocity, was 3.4 injector diameters (3.46 mm). Figure 4 also shows a theoretically determined boundary-layer velocity profile. This profile was obtained by use of flat-plate laminar-skin-friction calculations to an assumed boundary-layer transition point $\left(R_x = 2.90 \times 10^6\right)$, followed by the turbulent boundary-layer solution discussed in reference 20.

		δ/D	δ^*/D	θ_B/D
○	Exp.	3.400	1.498	0.193
——	Theo.	3.560	1.358	0.162
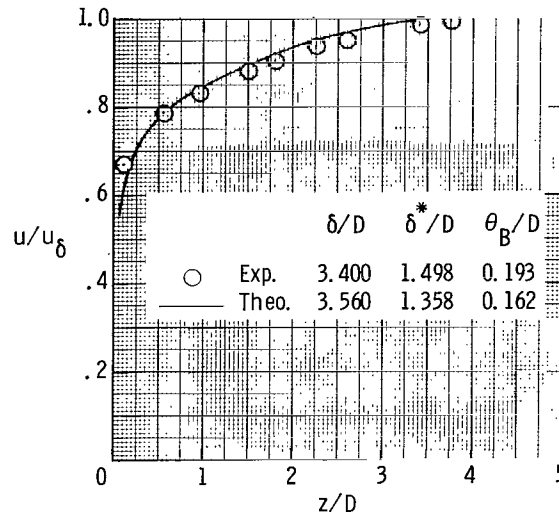
Figure 4.- Boundary-layer velocity distribution. No injection;
$\dfrac{x}{D} = 0$; $R_e = 6.19 \times 10^7$ per meter.

Plate Static Pressures

Undisturbed plate static pressures were found to be slightly higher than tunnel static pressure because of a misalinement of the plate of approximately 0.8°. Thus the boundary-layer-edge Mach number at the injector station was 4.04 throughout the investigation; this compares with a tunnel Mach number of 4.05.

Figure 5 presents the nondimensional static pressure distribution along the plate center line for the four injectors (injection angles) tested. Pressures measured between adjacent injectors (between jets) are represented by the solid symbols. These data show a region of high pressure in the vicinity of the injector, followed by a low pressure overshoot and a gradual return to the undisturbed pressure. The magnitude of the pressure rise increases for more normal injection angles. Experimental observations made during other tests (ref. 14) have shown that the overpressure ahead of the jet represents a region of boundary-layer separation. Variations in the jet-induced boundary-layer separation
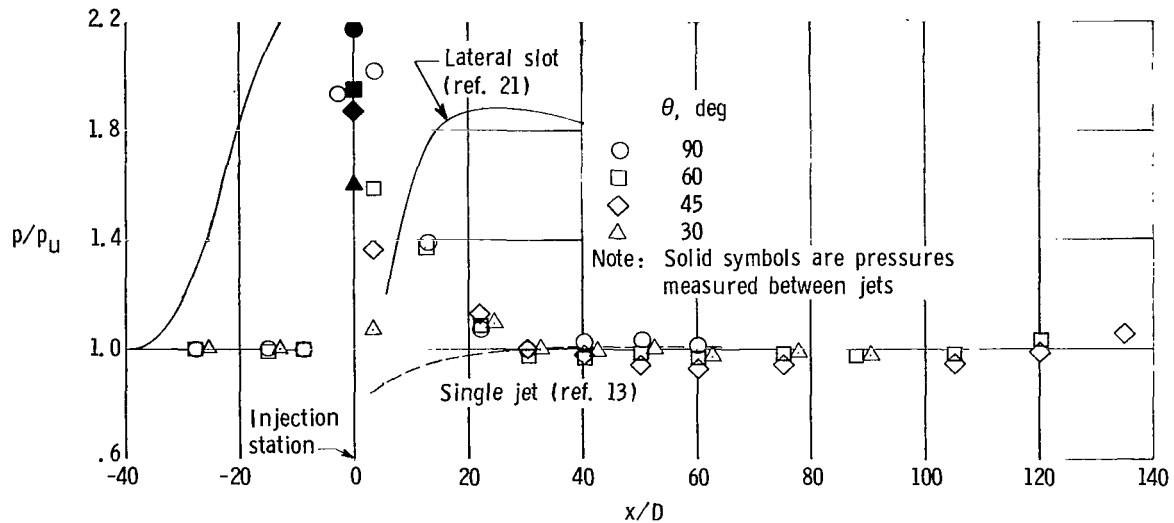
Figure 5.- Axial center-line static pressure.

ahead of the injector resulting from different injection angles could not be distinguished with the limited number of static-pressure orifices located in this area.

The flow separation in the region ahead of the injector station (fig. 5) was observed for both the single jet of reference 13 and the lateral-slot injector of reference 21. In the downstream region, however, the single jet produced a low pressure, shown by the broken line in figure 5, whereas the two-dimensional lateral-slot injector produced an extensive region of high pressure, shown by the solid line in figure 5. Although the test conditions $\left(M_\infty = 11.8; \ \dfrac{p_j}{p_\infty} = 3 \right)$ for the lateral-slot investigation are not similar to the present test conditions, the results depict representative trends. The low pressure from the single-jet data results from the flow expansion and acceleration around the lee side of the jet, and the overpressure depicts continued flow separation. The size of the disturbed region apparently depends on the condition and thickness of the boundary layer. Because of the large longitudinal pressure gradients, surveys between the injector station and the station $\dfrac{x}{D} = 30$ would be inaccurate.

Vertical Survey Data

Nondimensional profiles of hydrogen concentration and total pressure reduced from the vertical-survey data are presented in figures 6 and 7, respectively, for all survey stations (x/D) and injection angles (θ). Selected single-jet data from reference 11 have been included in both figures. In figure 6 the present hydrogen-concentration data are represented by the symbols and the single-jet data are represented by the dashed curve and shaded region. Hydrogen-concentration values are nondimensionalized by the maximum
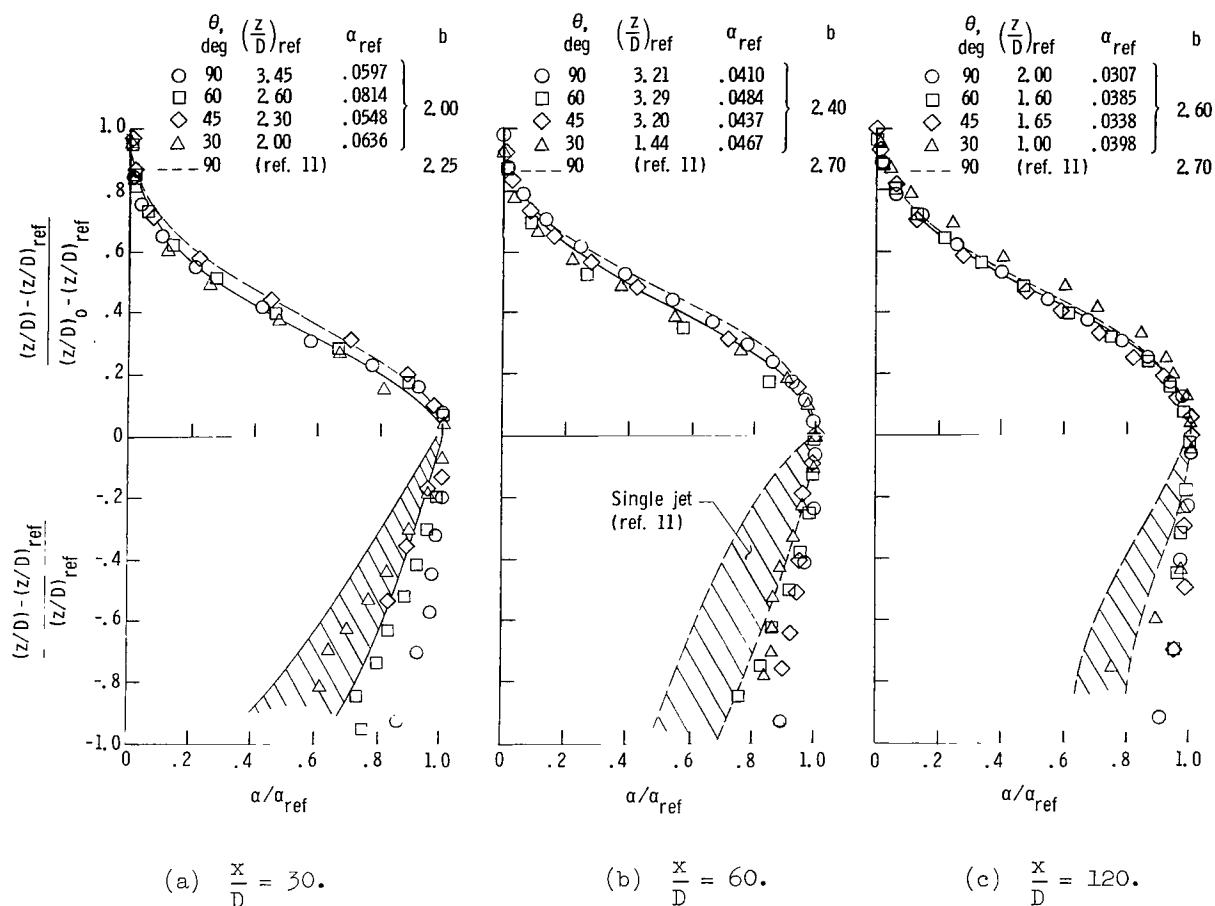
9

Figure 6. Data tables for three panels:

θ, deg	$\left(\frac{z}{D}\right)_{ref}$	α_{ref}	b
○ 90	3.45	.0597	
□ 60	2.60	.0814	2.00
◇ 45	2.30	.0548	
△ 30	2.00	.0636	
--- 90	(ref. 11)		2.25

θ, deg	$\left(\frac{z}{D}\right)_{ref}$	α_{ref}	b
○ 90	3.21	.0410	
□ 60	3.29	.0484	2.40
◇ 45	3.20	.0437	
△ 30	1.44	.0467	
--- 90	(ref. 11)		2.70

θ, deg	$\left(\frac{z}{D}\right)_{ref}$	α_{ref}	b
○ 90	2.00	.0307	
□ 60	1.60	.0385	2.60
◇ 45	1.65	.0338	
△ 30	1.00	.0398	
--- 90	(ref. 11)		2.70

Single jet (ref. 11)

(a) $\frac{x}{D} = 30.$ (b) $\frac{x}{D} = 60.$ (c) $\frac{x}{D} = 120.$

Figure 6.- Nondimensional profiles of hydrogen concentration from vertical-survey data.

concentration measured on each profile. The vertical height above the plate to this peak concentration $(z/D)_{ref}$, which was chosen as the origin of the nondimensional vertical coordinate system, and the vertical distance to the point of zero hydrogen concentration $(z/D)_0$ are used to nondimensionalize the vertical coordinate. In the upper region above the point of peak concentration, the profile resembles coaxial mixing profiles and can be correlated well by a Gaussian exponential curve of the form

$$\frac{\alpha}{\alpha_{ref}} = \exp\left\{-5\left[\frac{\frac{z}{D} - \left(\frac{z}{D}\right)_{ref}}{\left(\frac{z}{D}\right)_0 - \left(\frac{z}{D}\right)_{ref}}\right]^b\right\} \tag{1}$$

where b, the profile shape index, generally depends only on the downstream location of the survey station. This same result was obtained for single-jet studies reported in reference 11 and is shown in figure 6 by the broken curve. The solid curves in figure 6 are
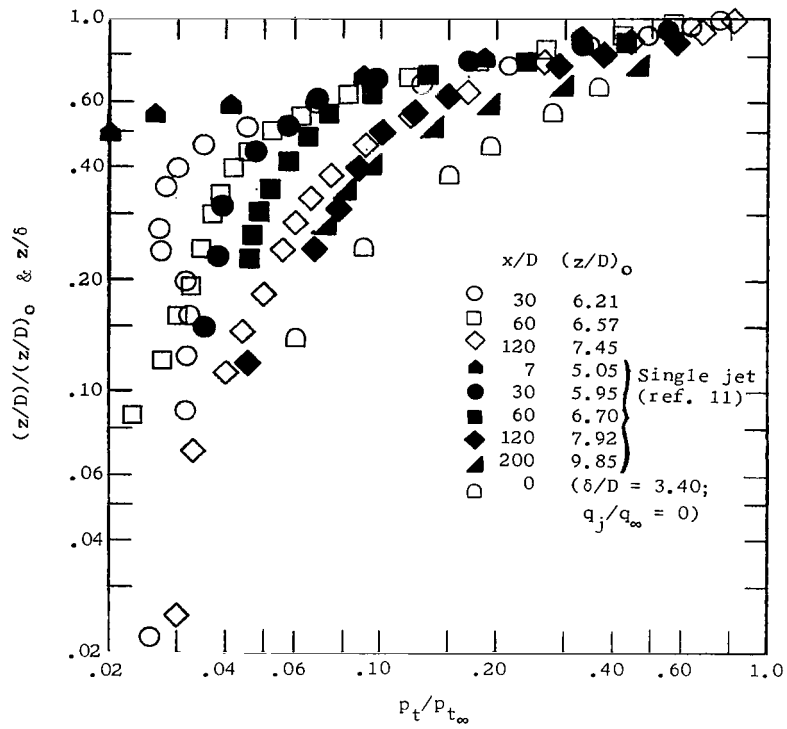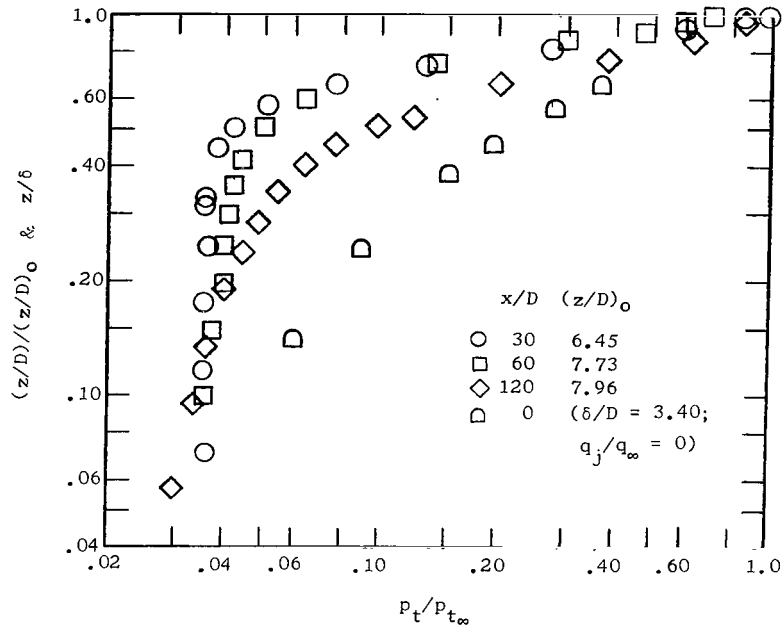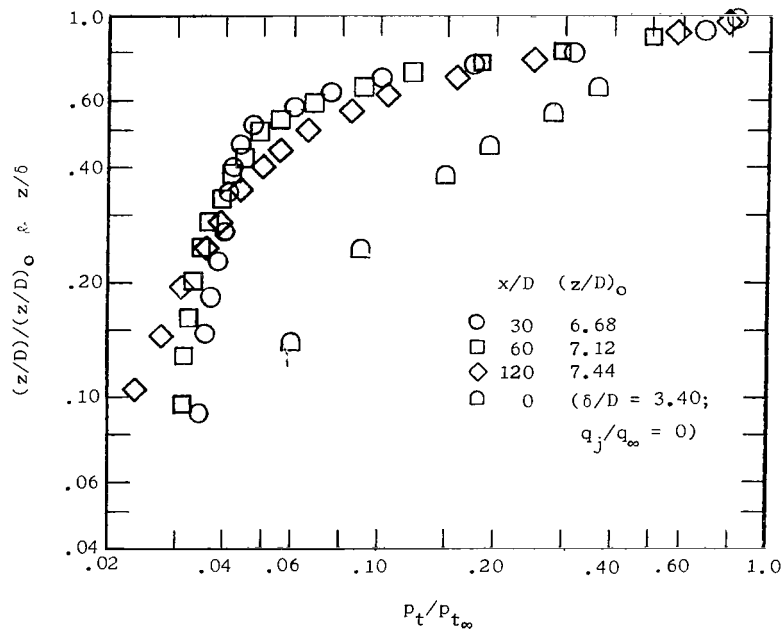
(a) $\theta = 90°$.
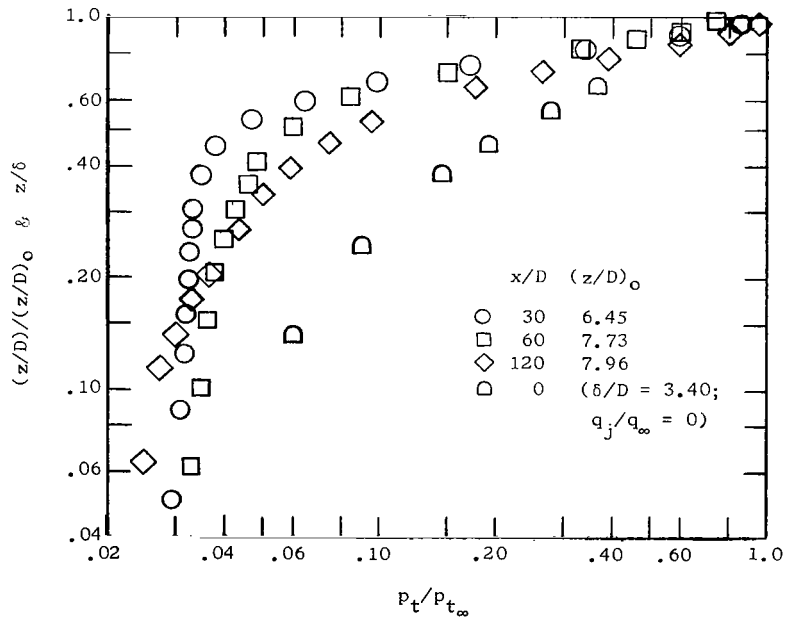
(b) $\theta = 60°$.

Figure 7.- Nondimensional profiles of total pressure from vertical-survey data.

(c) $\theta = 45°$.

(d) $\theta = 30°$.

Figure 7.- Concluded.

data correlations using equation (1), with b as listed on each figure. The values of b for the single-jet data are slightly higher than those for the data of the present investigation. No consistent deviation from the correlation line can be determined as a function of injection angle.

In the lower region of figure 6 between the plate surface and $\left(\dfrac{z}{D}\right)_{ref}$, the injection angle affects the uniformity of the concentration profiles at an x/D of 60 and less, with the more uniform profiles occurring for the higher injection angles. Downstream of the station $\dfrac{x}{D} = 60$ the profile shape is not affected by the injection angle, with the exception of the results for $\theta = 30^O$ near the surface (fig. 6(c)). However, these results (two data points) are considered to be in error because of the trends shown by the remainder of the profile. The profile shape in the lower region appears to be a measure of adjacent-jet interaction. For no lateral interference, the single-jet profile, represented by the shaded region, continues to decrease towards the plate; whereas, for the present jet spacing, the adjacent-jet mixing regions interact by the last station. Also, the higher injection angles produce interference between adjacent-jet mixing regions at stations nearer to the injectors.

Figure 7 compares the nondimensional total-pressure profiles from the vertical surveys with the undisturbed boundary-layer profile at the injector station. The vertical coordinate is nondimensionalized by the corresponding values of $(z/D)_0$ or the boundary-layer thickness δ. Single-jet total-pressure profiles from reference 11 are represented in figure 7(a) by the solid symbols. These data are for normal injection of hydrogen at q_j/q_∞ of unity.

Both the single-jet and the multiple-jet data show the largest pressure loss at the survey station nearest to the injector. As the mixing proceeds downstream, the total-pressure profile shape approaches that of the undisturbed boundary layer as a result of higher total-pressure air entering the mixing region. The normal multiple jet produces the most severe pressure loss near the injector station. However, the shape of the pressure profile approaches that of the undisturbed profile more rapidly as the flow proceeds downstream than do the corresponding shapes of the profiles for lower injection angles. The single jet has relatively low blockage and produces about the same pressure profile at an x/D of 30 (fig. 7(a)) as the pressure profile measured for the multiple-jet case of $\theta = 30^O$ (fig. 7(d)).

In order to illustrate the effect of injection angle θ on the pressure recovery p_r, a comparison of total-pressure profiles is presented in figure 8. The profiles presented are for the present multiple-jet data at $\dfrac{x}{D} = 30$, the single-jet data at $\dfrac{x}{D} = 30$ (from fig. 7(a)), and the undisturbed boundary-layer data at $\dfrac{x}{D} = 0$. The mass averaged total
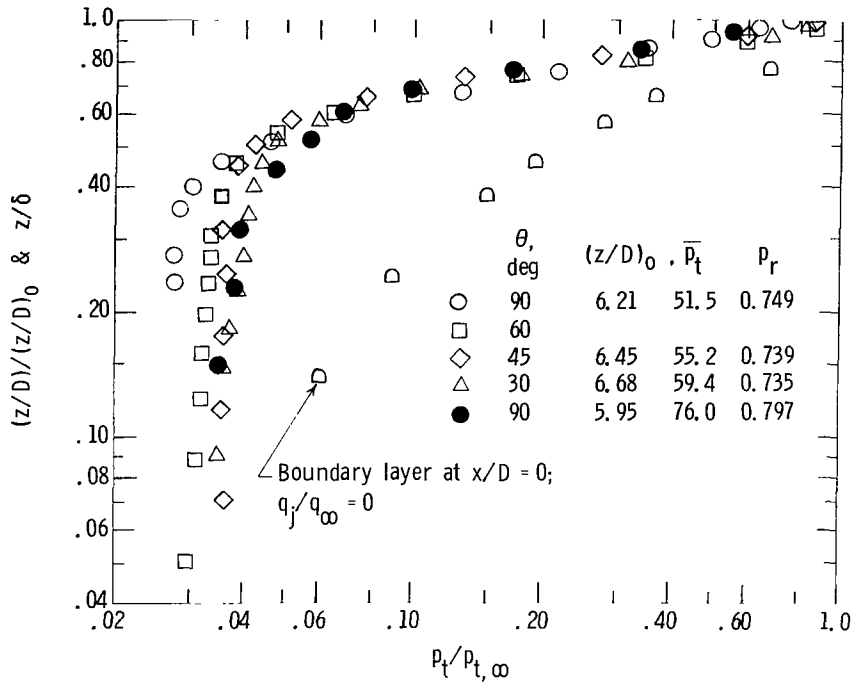
θ, deg	$(z/D)_0$	$\bar{p}_t$	P_r
○ 90	6.21	51.5	0.749
□ 60			
◇ 45	6.45	55.2	0.739
△ 30	6.68	59.4	0.735
● 90	5.95	76.0	0.797

Boundary layer at $x/D = 0$; $q_j/q_\infty = 0$

Figure 8.- Comparison of total-pressure profiles. $\frac{x}{D} = 30$.

pressures $(\bar{p}_t)$ were determined by integration of the jet mixing contours and were non-dimensionalized by $\bar{p}_t$ of the undisturbed flow at the injection station that contained the same air mass flow as the downstream mixing region. Although variations exist in the vertical profile shape, the average total-pressure recovery is approximately the same for each tested injection angle, with a slight decreasing trend for lower injection angles. The pressure recovery for $\theta = 60°$ was not obtained because of instrumentation error.

The total-pressure loss is associated with the loss in momentum of the air in furnishing the injected hydrogen with axial momentum during the mixing process. Since the lower-injection-angle jets already have some axial momentum, they do not lower the air total pressure so much as do the normal jets.

Flow Contours

Typical contours of hydrogen mass fraction, hydrogen flow rate, and air flow rate are presented in figures 9(a), 9(b), and 9(c), respectively. These contours were determined by cross plotting the vertical and horizontal profiles at constant values of the particular contour parameter; these contours represent a cross section of the mixing-region flow in the YZ-plane. Note that the vertical scale is double the horizontal scale. The symbols on each contour are not data points; but since the symbols result from the cross-plot procedure, they are left on the figure to identify the contours. The outer edge of the

14
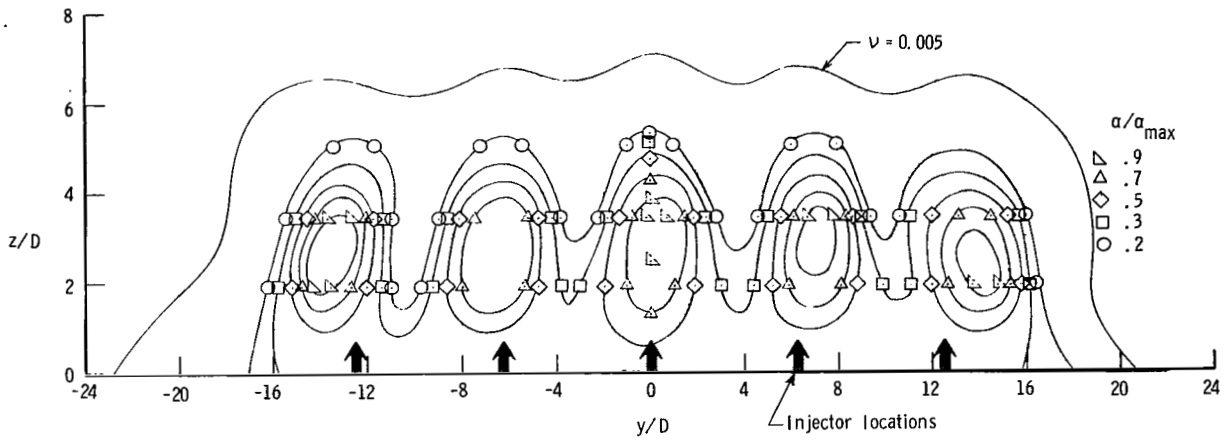
(a) Hydrogen mass fraction.
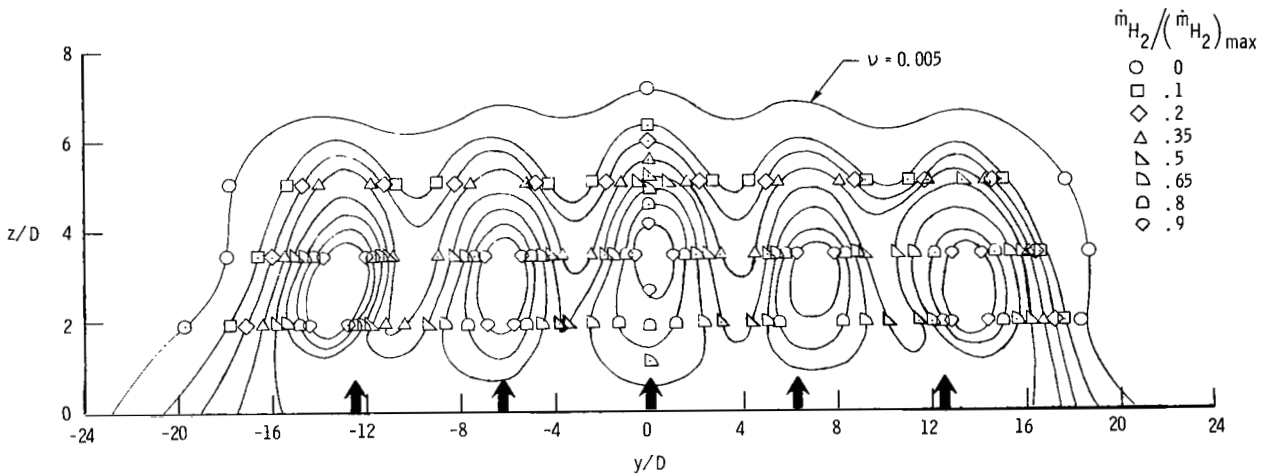
(b) Hydrogen flow rate.
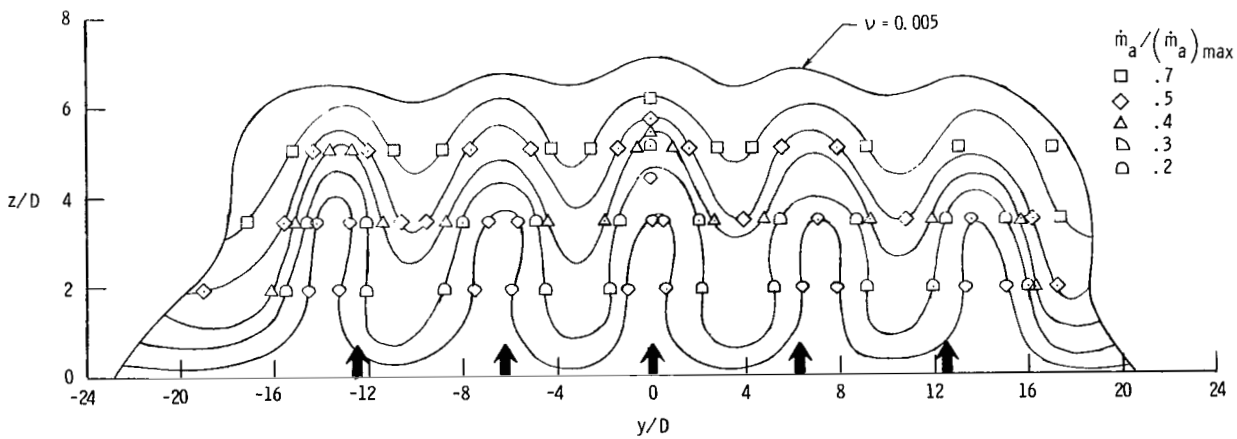
(c) Air flow rate.

Figure 9.- Typical flow contours. $\frac{X}{D} = 30$; $\theta = 30°$.

mixing region is defined by the contour for hydrogen volume fraction (ν) of 0.005. The contours produced by the three central jets are quite similar in appearance, but some lateral spreading of the concentration peaks has resulted because of unrestrained lateral mixing of the end jets. The center-jet mixing region has a relatively small amount of spreading and provides a good simulation of the mixing region downstream of a continuous row of laterally spaced fuel injectors. For reference, contours of the central-jet mixing region for all cases are presented in figures 17 to 19 of the appendix. The important results obtained from the contours are hydrogen penetration and mixing rate, which are discussed in the following paragraphs.

Penetration

A sketch of the flow field resulting from the interaction of a secondary wall jet with a supersonic free stream is presented in figure 10. This sketch illustrates several methods used in the literature to define the jet penetration P. The most widely used measure is associated with the initial penetration, for example, h_{top} and h_{mid}, which correspond to the top and center of the jet Mach disk. Values of these jet details are easily obtained from schlieren photographs and have primary applications to nonfuel injection and mixing problems. For fuel-injection studies the downstream fuel distribution, illustrated by the mixing-region cross section, is more important than the initial penetration. In this report the fuel distribution will be measured by two nondimensionalized parameters, as illustrated in figure 10. The measure P/D, referred to as simply as the penetration, is the vertical distance from the plate to the edge of the mixing region (ν = 0.005); the other measure $(z/D)_{\alpha_{max}}$, referred to as the maximum-concentration trajectory, is the distance from the plate to the point of maximum concentration. Values of P/D and $(z/D)_{\alpha_{max}}$ were determined from the flow contours in the appendix (figs. 17 and 18) and are not necessarily on the vertical survey.
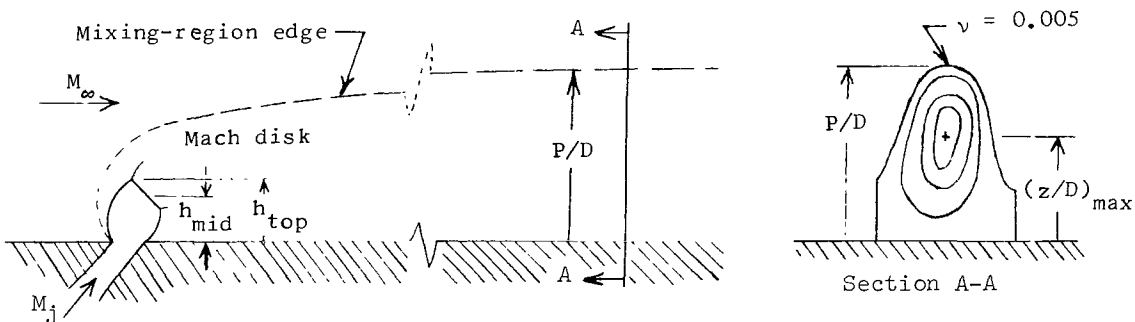

Figure 10.- Sketch of flow field.

Penetration results are presented in figure 11 as a function of downstream distance. The results for normal injection and injection of 30° can be represented by individual straight lines on this semilog plot, which is consistent with previous correlations (refs. 11, 13, 15, 16, and 18). Although there is some scatter for $\theta = 45°$ and $\theta = 60°$, the overall trend of the data indicates increased (greater) penetration for lower injection angles, as illustrated by the family of straight lines. Single-jet-data correlations from references 11 and 15 are also presented in figure 11.
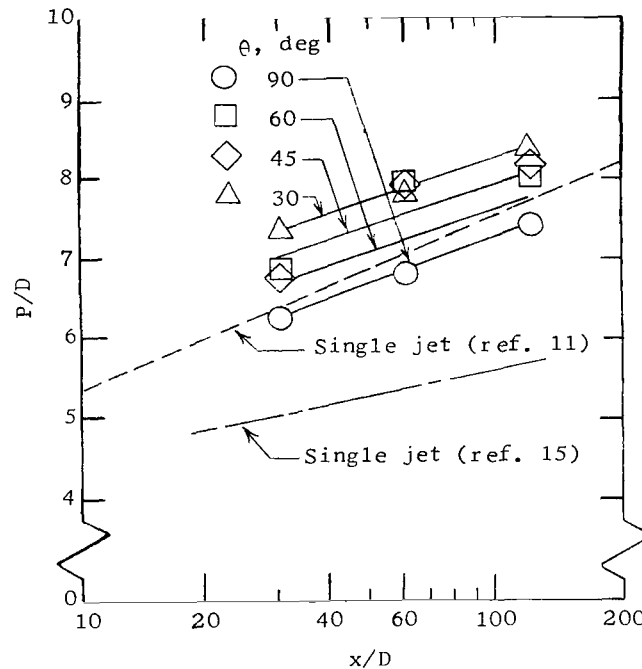
Figure 11.- Penetration results.

The sonic injection of hydrogen from a flat plate into a Mach 4.03 free stream has been studied in reference 11. The penetration correlation is presented in notation of the present paper as follows:

$$\frac{P}{D} = 3.87 \left(\frac{q_j}{q_\infty}\right)^{0.300} \left(\frac{x}{D}\right)^{0.143} \tag{2}$$

for $0.5 \leq \dfrac{q_j}{q_\infty} \leq 1.5$ and $7 \leq \dfrac{x}{D} \leq 120$. Data obtained by normal injection of helium from a 0.95-cm-diameter sonic jet into an 8.9-cm-cylindrical test section have been presented in reference 15. The penetration correlation is expressed as (also in notation of present paper)

17

$$\frac{P}{D} = 3.75 \left(\frac{q_j}{q_\infty}\right)^{0.50} \left(\frac{x}{D}\right)^{0.0866} \tag{3}$$

The relative size of the hydrogen jet and the test section for tests of reference 15 were such that the jet may have been restricted in its lateral spreading by the curvature of the wall. However, the variation in the penetration correlations of equation (2) and equation (3) is believed to result primarily from differences in the ratio of boundary-layer thickness to jet diameter. Unreported NASA data indicate that for sonic injection of hydrogen from a single jet the ratio of boundary-layer thickness to jet diameter has a significant effect on the penetration, with greater penetration resulting from thicker boundary layers. The results represented by equation (2) (ref. 11) were obtained with the value of δ/D slightly less than for the present case whereas the results represented by equation (3) (ref. 15) appear to have a very small value of δ/D. Although the combustor boundary-layer thickness was not given in reference 15, the short combustor length and relatively large jet diameter suggest the existence of a small value of δ/D.

The maximum-concentration trajectories for the present tests are presented in figure 12 and show greater values of $(z/D)_{\alpha_{max}}$ for lower injection angles. The trajectory $(z/D)_{\alpha_{max}}$ generally increases in the region $30 \leq \frac{x}{D} \leq 60$ and then decreases to $\frac{x}{D} = 120$. References 11 and 15 also present single-jet results of the maximum-concentration trajectory $(z/D)_{\alpha_{max}}$. The flat-plate results (ref. 11) are represented by the dashed curve in figure 12 and the cylindrical-test-section results (ref. 15) are represented by the solid curve which is of the form

$$\left(\frac{z}{D}\right)_{\alpha_{max}} = 3.45 \left(\frac{q_j}{q_\infty}\right)^{0.533} \left(\frac{x}{D}\right)^{-0.259} \tag{4}$$

The flat-plate single-jet results have an increasing maximum-concentration trajectory with downstream distance; the cylindrical-test-section results have a decreasing maximum-concentration trajectory. The shape of the concentration profiles presented in reference 15 indicates that the curvature of the test-section walls restricted the lateral diffusion of the hydrogen, thus confining turbulent diffusion to the vertical direction which resulted in the maximum-concentration trajectory approaching the wall. The single-jet flat-plate case, on the other hand, imposed no lateral restrictions on the mixing, and the maximum-concentration trajectory increased with downstream distance. For the multiple-jet data of the present test the fuel initially mixed laterally, which increased the maximum-concentration trajectory. Downstream of the station $\frac{x}{D} = 60$ the adjacent-jet interaction

18

restricted the lateral spreading and the fuel mixed upward; as a result, the maximum-concentration trajectory turned and approached the wall.
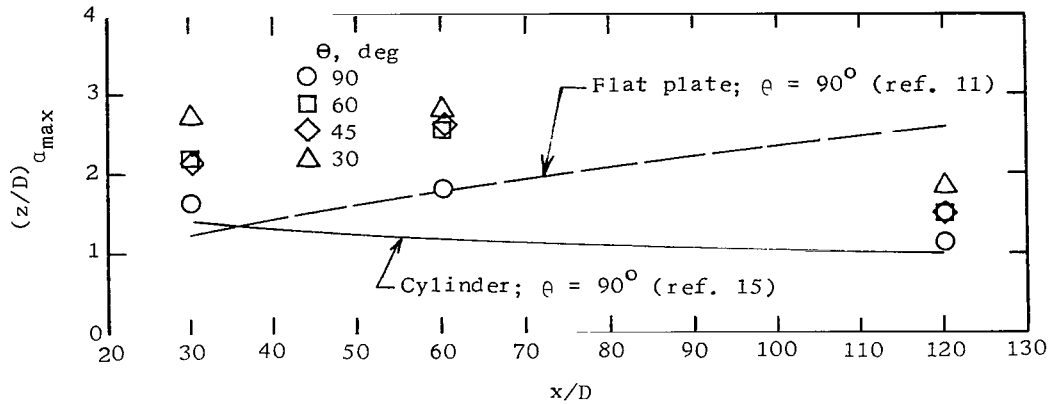

Figure 12.- Maximum-concentration trajectories.

Two studies of injection-angle effect on jet penetration (refs. 6 and 7) have shown that the initial jet penetration $\left(i.e., h_{top}/D \text{ or } h_{mid}/D\right)$ is proportional to the injection angle θ. In reference 15, which contains a study of the downstream fuel (helium) distribution in a circular, confined duct, the various injection-angle results were correlated by

$$\frac{P}{D} = 1.56\left(\frac{\rho_j}{\rho_\infty}\right)^{0.468}\left(\frac{u_j}{u_\infty}\right)^{0.946}(\sin \theta)^{0.844}\left(\frac{M_j}{M_\infty}\right)^{-0.56}\left(\frac{x}{D}\right)^{0.0866} \tag{5}$$

The authors thereby contend that the penetration is governed by the normal component of the jet dynamic pressure $q_j \sin \theta$. Although this correlation would be expected to apply for the initial jet penetration $\left(h_{top}/D\right)$, the other jet component would be expected to enter into the correlation of the downstream fuel distribution. Since the secondary jet is turned downstream because of the difference between its downstream component of total momentum (or dynamic pressure $q_j \cos \theta$) and the airstream momentum (or dynamic pressure q_∞), the normal component retains more of its initial momentum if the absolute value of $q_\infty - q_j \cos \theta$ is small. Therefore, the correlation of equation (5) is extended by introducing the effective-dynamic-pressure ratio

$$\left(\frac{q_j}{q_\infty}\right)_{eff} = \frac{q_j \sin \theta}{q_\infty - q_j \cos \theta} = \frac{\dfrac{q_j}{q_\infty} \sin \theta}{1 - \dfrac{q_j}{q_\infty} \cos \theta} \tag{6}$$

19

For normal injection the effective-dynamic-pressure ratio $\left(q_j/q_\infty\right)_{eff}$ reduces to the dynamic-pressure ratio q_j/q_∞; but as the injection angle is reduced from 90°, the effective-dynamic-pressure ratio increases for a constant q_j/q_∞. The maximum value of this parameter is obtained by variation of q_∞, q_j, and θ such that

$$q_j \cos \theta \to q_\infty \tag{7}$$

where θ is not zero. Within the range of the present tests, $\left(q_j/q_\infty\right)_{eff}$ is maximum for $\theta = 30^O$.

The effective-dynamic-pressure ratio was used to correlate the penetration and the maximum-concentration-trajectory results. Figure 13 presents data correlations of the multiple-jet penetration data from figure 11 in terms of the effective-dynamic-pressure ratio. The data have been correlated by the equation

$$\frac{P}{D} = 3.385\left(\frac{q_j}{q_\infty}\right)_{eff}^{0.09} \left(\frac{x}{D}\right)^{0.18} \tag{8}$$

which is of the same form as the correlations presented by equation (2) and equation (3). The variation with downstream distance is about the same as was shown for the single-jet flat plate (eq. (2)). Equation (8) implies that the maximum penetration occurs when the downstream component of jet dynamic pressure is equal to the free-stream dynamic pressure. However, for the present conditions, $\dfrac{q_j}{q_\infty} = 1.0$, the equation is mathematically undefined at this point ($\theta = 0$).
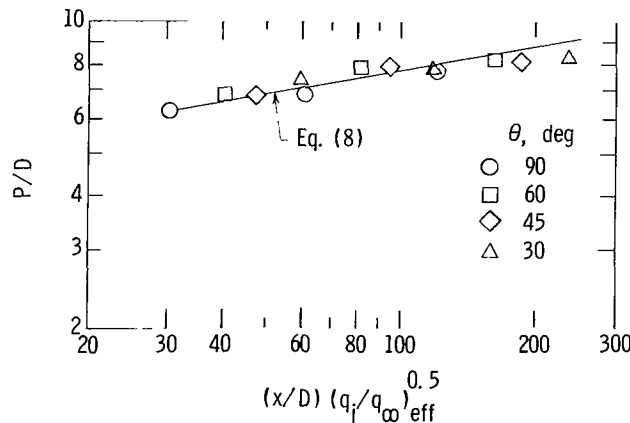
Figure 13.- Penetration correlation.

The single-jet maximum-concentration trajectories were correlated in reference 11

by plotting $\dfrac{z}{D}\left(\dfrac{q_j}{q_\infty}\right)^{-0.3}$ versus x/D (symbol notation of present paper), thereby collaps-

ing the data for the various ratios q_j/q_∞ to the ratio $\dfrac{q_j}{q_\infty} = 1.0$. A similar approach is

used herein to correlate the present data. Results for all the injection angles were col-

lapsed onto the normal injection results by plotting $\dfrac{z}{D}\left(\dfrac{q_j}{q_\infty}\right)^{-0.38}_{\text{eff}}$ versus x/D in

figure 14.
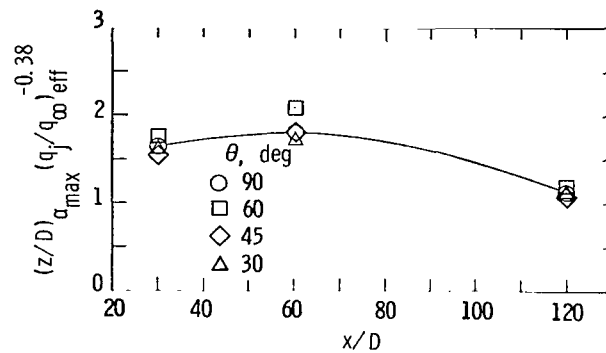
Figure 14.- Maximum-concentration-trajectory correlation.

Maximum Concentration

The maximum hydrogen mass fraction measured for each profile, which is a gage
of the mixing rate, is presented in figure 15 as a function of the downstream station for
each angle of injection. Data scatter (on the order of ±10 percent) results from the
inability to position the probe at the exact point of maximum concentration. The results
of the normal injection angle $\theta = 90^\circ$ and the injection angle $\theta = 30^\circ$ are represented
by the two faired lines in figure 15. Because of the considerable data scatter for $\theta = 45^\circ$
and $\theta = 60^\circ$, these injection angles will not be considered in this discussion. Comparing
the results for $\theta = 90^\circ$ and $\theta = 30^\circ$ shows two trends associated with changing the
injection angles. The lower angles produce a lower maximum concentration and a slightly
faster rate of decay throughout the mixing region surveyed. Also presented in figure 15

are single-jet data for normal injection at $\dfrac{q_j}{q_\infty} = 1.0$ from reference 11. The rate of

decay of the maximum concentration is slower in the downstream region $\left(30 \leq \dfrac{x}{D} \leq 120\right)$

for multiple-jet data than for single-jet data. However, the initial mixing rate is more

rapid for the multiple-jet injection as seen at the station $\dfrac{x}{D} = 30$ where the maximum

hydrogen concentration is two-thirds that for the single jet. This faster initial mixing

apparently results from the increased flow turbulence caused by the initial interaction between adjacent-jet flow fields.

Reference 22 has shown that for coaxial injection, the maximum concentration in the downstream region decays at a rate proportional to $(x/D)^{-2.0}$. In figure 15 the decay rate of the single-jet and multiple-jet injection is proportional to $(x/D)^{-0.8}$ and $(x/D)^{-0.35}$, respectively. These variations in maximum-concentration decay rates are indicative of the limitation imposed on the turbulent mixing phenomenon by a solid boundary and by adjacent jets.
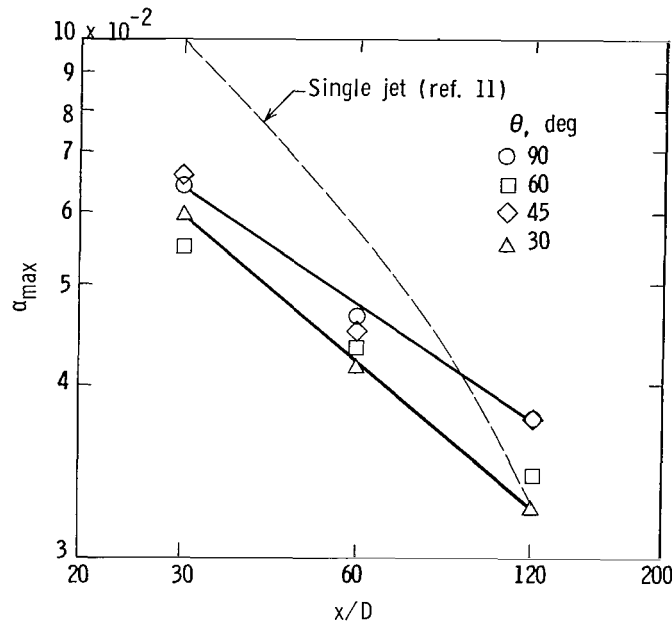
Figure 15.- Maximum hydrogen mass fraction as a function of survey station.

Maximum-concentration decay is correlated in figure 16 using the effective-dynamic-pressure ratio. The data are correlated by

$$\alpha_{max} = 0.20 \left[\left(\frac{q_j}{q_\infty} \right)_{eff}^{0.22} \frac{x}{D} \right]^{-0.350} \tag{9}$$

Equation (9) correlates the results within a maximum data scatter of 15 percent.
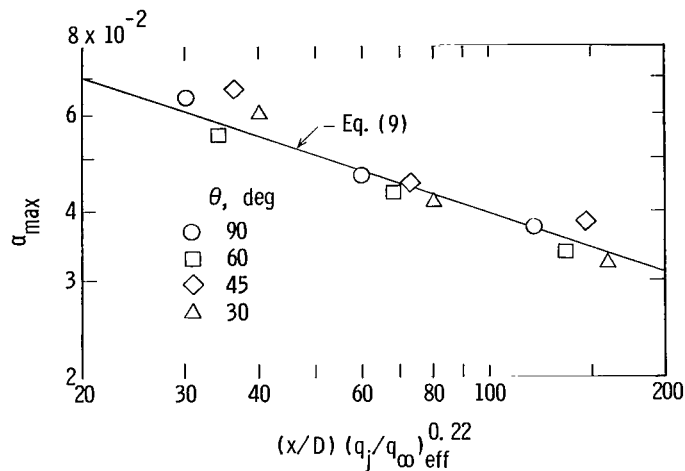
Figure 16.- Correlation of the maximum-concentration decay.

CONCLUDING REMARKS

Although the investigation primarily examined the effect of injection angle on multiple-jet mixing, differences between multiple-jet and single-jet mixing were also determined by comparison with single-jet data.

The following trends were observed in the downstream mixing region as a result of decreasing the injection angle:

(1) Increase at the downstream stations in penetration and the height of the maximum-concentration trajectory

(2) Faster mixing as measured by the maximum-hydrogen-concentration decay

(3) Reduction in the flow disturbance measured by wall pressures directly behind the jet

(4) Slight improvement in total pressure in the mixing region

These results are explained by consideration of the airstream momentum loss associated with turning the hydrogen jet downstream. The lower injection angles require less additional axial momentum and, therefore, produce less flow disturbance and total-pressure loss. Consideration of methods of correlating jet- and air-momentum effects resulted in the use of an effective-dynamic-pressure ratio to correlate penetration and maximum-hydrogen-concentration results. The successful use of this parameter implies that optimum penetration would result when the initial axial components of the fuel and air momentum are identical.

When compared with single-injector data, the multiple-injector data resulted in the following trends:

(1) Wall pressures directly behind the center jet were higher than undisturbed plate pressures, whereas the single jet produced a low-pressure expansion region

(2) More uniform concentration distributions were obtained below the point of maximum concentration

(3) The air flow sustained greater total-pressure losses

(4) The maximum-concentration trajectory approached the wall with downstream distance at injector stations (x/D) greater than 60; whereas, the trajectory continued to rise for the single jet

(5) The initial decay of the maximum concentration was faster

(6) The rate of decay of the maximum concentration in the region $30 \leqq \frac{x}{D} \leqq 120$ was slower

These observations apparently result from two flow phenomena associated with multiple jets. The first is the initial interference between jet flow fields. This interference cancels the air-flow expansions around the jets, adds turbulence to the initial mixing region, and produces increased total-pressure losses compared to the single-jet cases. The second flow phenomenon is the overlapping of the adjacent jet mixing regions. When these regions merge, the mixing of the hydrogen below the maximum concentration is restrained. The resulting fuel-air region is basically restricted to mixing in the vertical direction, resulting in the point of maximum concentration moving towards the wall. This laterally restricted mixing also results in the rate of decay of maximum concentration being slower in the downstream region.

Langley Research Center,
    National Aeronautics and Space Administration,
        Hampton, Va., February 2, 1972.

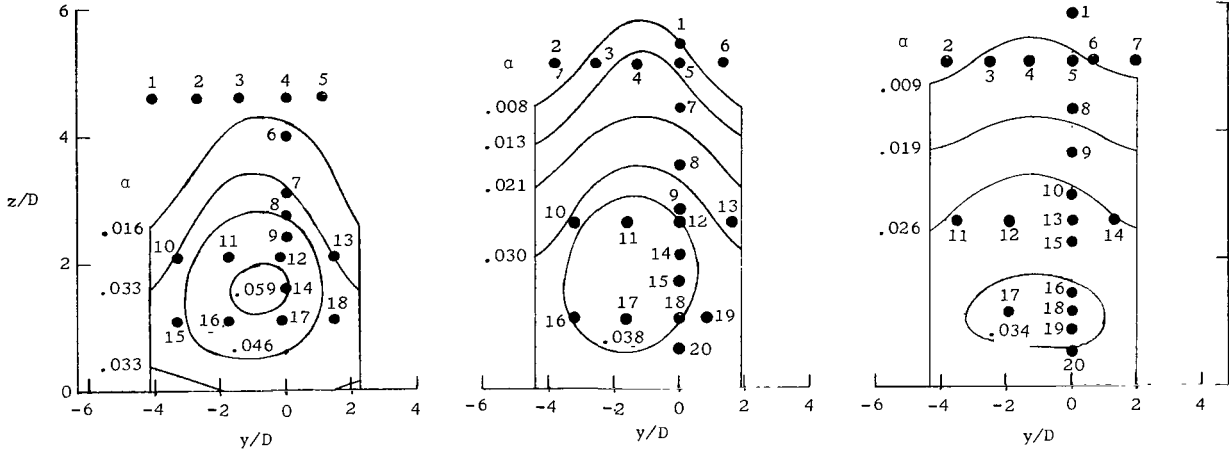## APPENDIX

CENTER-JET FLOW CONTOURS

Mixing-region contours of the center jet are presented in figures 17, 18, and 19 for hydrogen mass fraction, hydrogen flow rate, and air flow rate, respectively. The hydrogen-air mixing region for the center jet is defined by a zone 6.25 jet diameters wide, centered about the middle hydrogen concentration peak to give the most symmetrical concentration contour. Data points are included on the first contour in each of these figures to illustrate the accuracy of the flow contours. The contours show that the center-jet mixing region is not always alined with the center line of the plate; however, the lateral shift is small, with a maximum value of about 3 percent of the downstream distance.

x/D = 30;	α_{max} = 0.066				
●	α	●	α	●	α
1	.001	7	.037	13	.034
2	.005	8	.044	14	.049
3	.011	9	.048	15	.040
4	.009	10	.034	16	.055
5	.003	11	.058	17	.055
6	.019	12	.055	18	.044

x/D = 60;	α_{max} = 0.047				
●	α	●	α	●	α
1	.006	8	.028	15	.042
2	.006	9	.036	16	.043
3	.011	10	.035	17	.047
4	.014	11	.045	18	.043
5	.012	12	.040	19	.040
6	.006	13	.029	20	.006
7	.017	14	.041		

x/D = 120;	α_{max} = 0.037				
●	α	●	α	●	α
1	.005	8	.016	15	.032
2	.007	9	.022	16	.034
3	.010	10	.027	17	.037
4	.011	11	.027	18	.035
5	.010	12	.031	19	.035
6	.009	13	.030	20	.033
7	.007	14	.027		

(a)   θ = 90°.

x/D = 30; α_{max} = 0.063   x/D = 60; α_{max} = 0.044   x/D = 120; α_{max} = 0.036
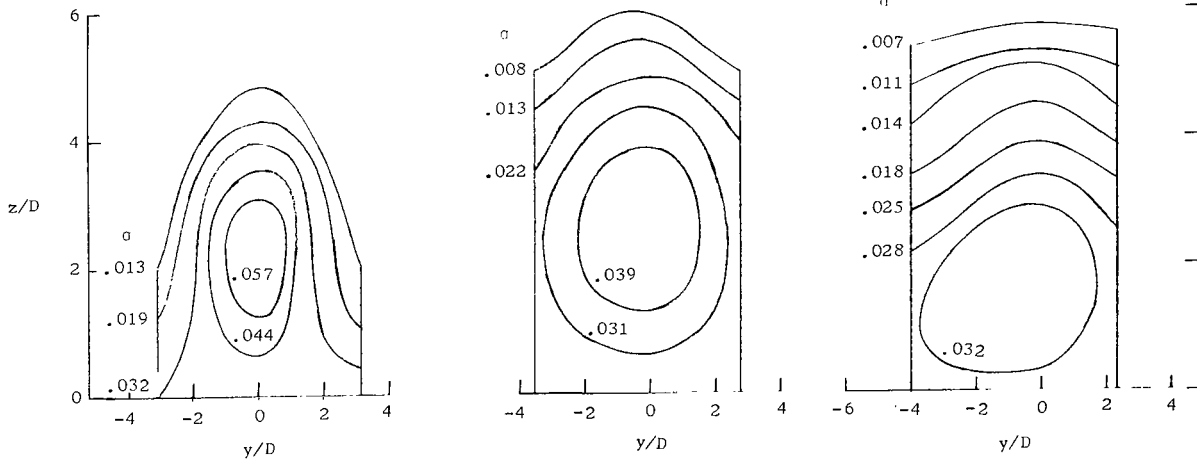
(b)   θ = 60°.

Figure 17.- Hydrogen concentration contours of center jet.

(c)   θ = 45°.

(d)   θ = 30°.
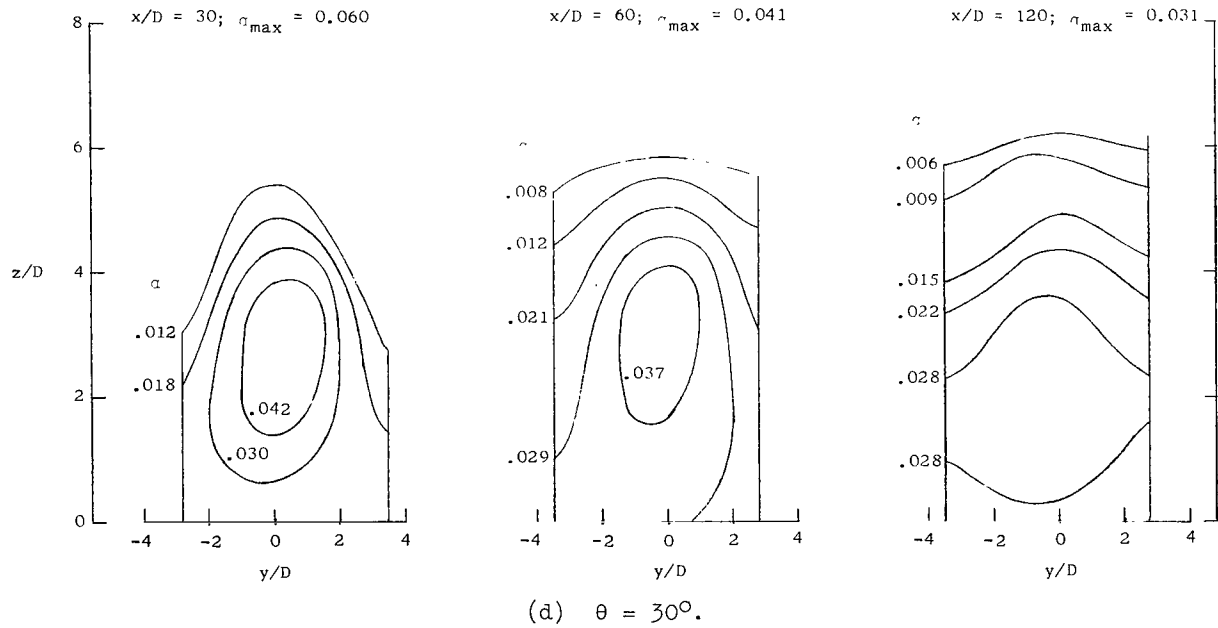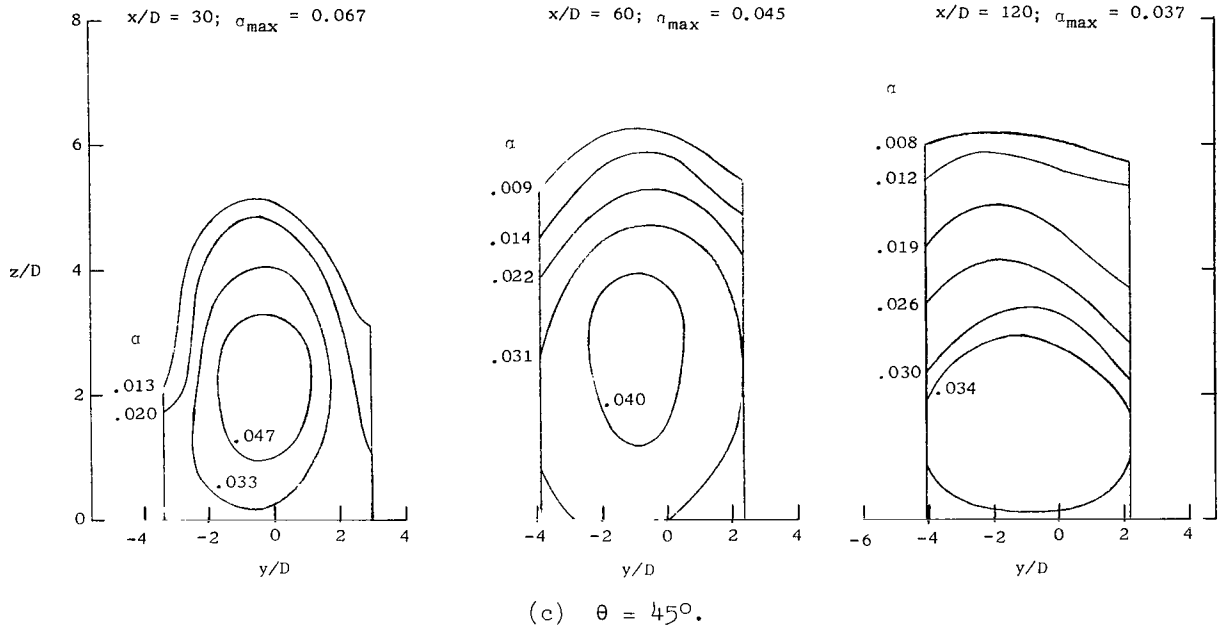
Figure 17.- Concluded.

x/D = 30;		$(\dot{m}_{H_2})_{max} = 3.11$			
●	$\dot{m}_{H_2}$	●	$\dot{m}_{H_2}$	●	$\dot{m}_{H_2}$
1	0.01	9	0.40	17	2.29
2	0.10	10	1.71	18	2.43
3	0.31	11	2.21	19	2.59
4	0.74	12	2.36	20	2.58
5	0.19	13	2.42	21	2.73
6	0.68	14	2.13	22	2.65
7	1.22	15	2.63	23	2.45
8	1.09	16	2.66		

x/D = 60;		$(\dot{m}_{H_2})_{max} = 2.75$			
●	$\dot{m}_{H_2}$	●	$\dot{m}_{H_2}$	●	$\dot{m}_{H_2}$
1	0.03	9	1.65	16	2.52
2	0.16	10	2.16	17	2.49
3	0.82	11	2.44	18	2.63
4	0.67	12	2.49	19	2.30
5	1.05	13	2.63	20	2.30
6	1.17	14	2.51	21	2.42
7	1.07	15	2.27	22	2.36
8	0.69				

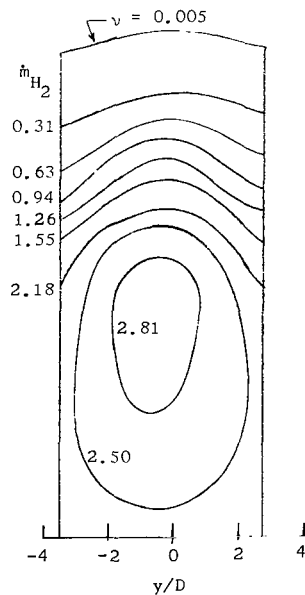| x/D = 120;		$(\dot{m}_{H_2})_{max} = 2.69$			
●	$\dot{m}_{H_2}$	●	$\dot{m}_{H_2}$	●	$\dot{m}_{H_2}$
1	0.12	9	1.05	16	2.18
2	0.41	10	1.97	17	2.68
3	0.91	11	2.31	18	2.63
4	1.05	12	2.52	19	1.76
5	1.24	13	2.15	20	1.85
6	1.33	14	2.09	21	2.41
7	1.27	15	2.12	22	2.10
8	1.21				
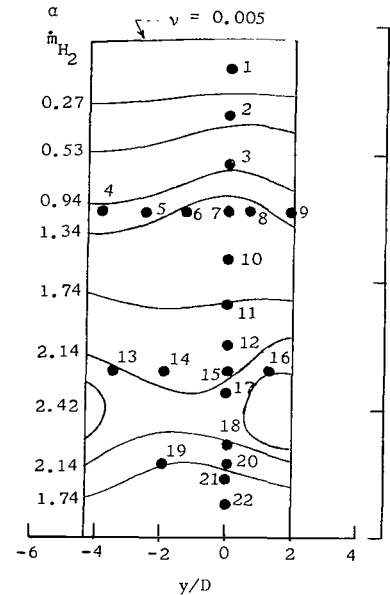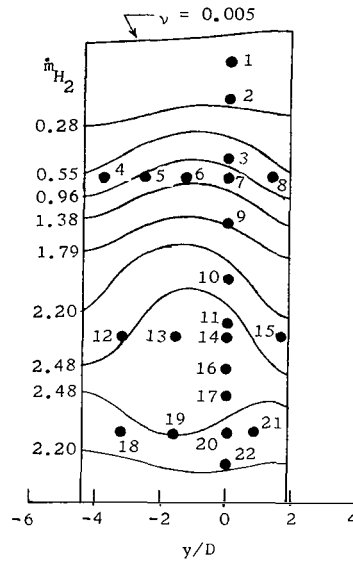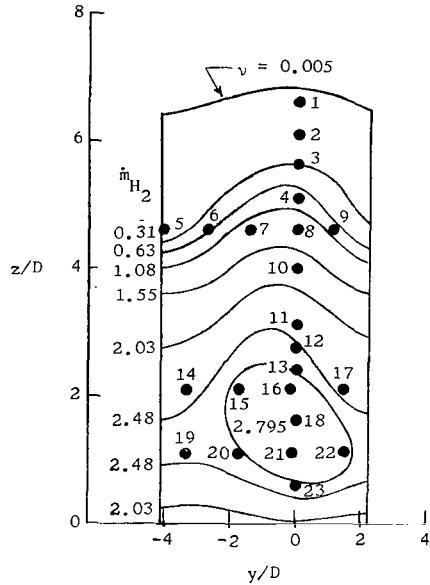
(a) θ = 90°.
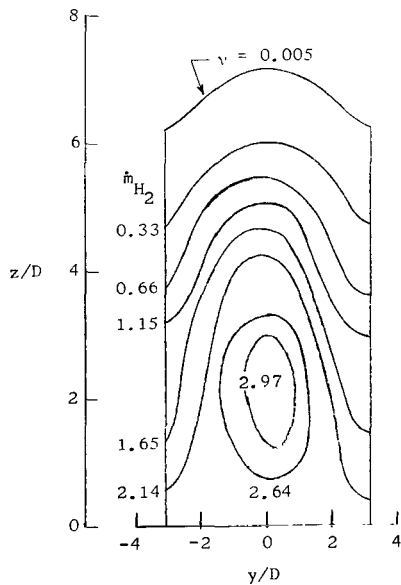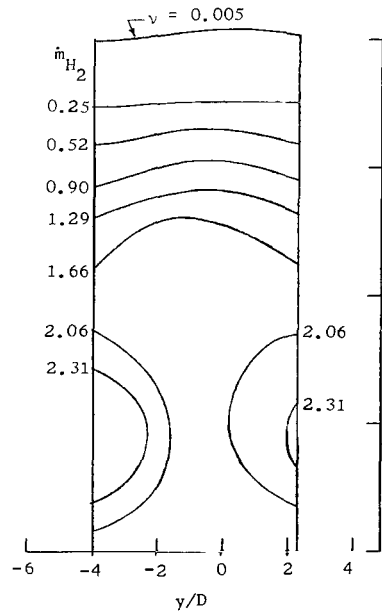
x/D = 30; $(\dot{m}_{H_2})_{max} = 3.28$ x/D = 60; $(\dot{m}_{H_2})_{max} = 3.12$ x/D = 120; $(\dot{m}_{H_2})_{max} = 2.58$
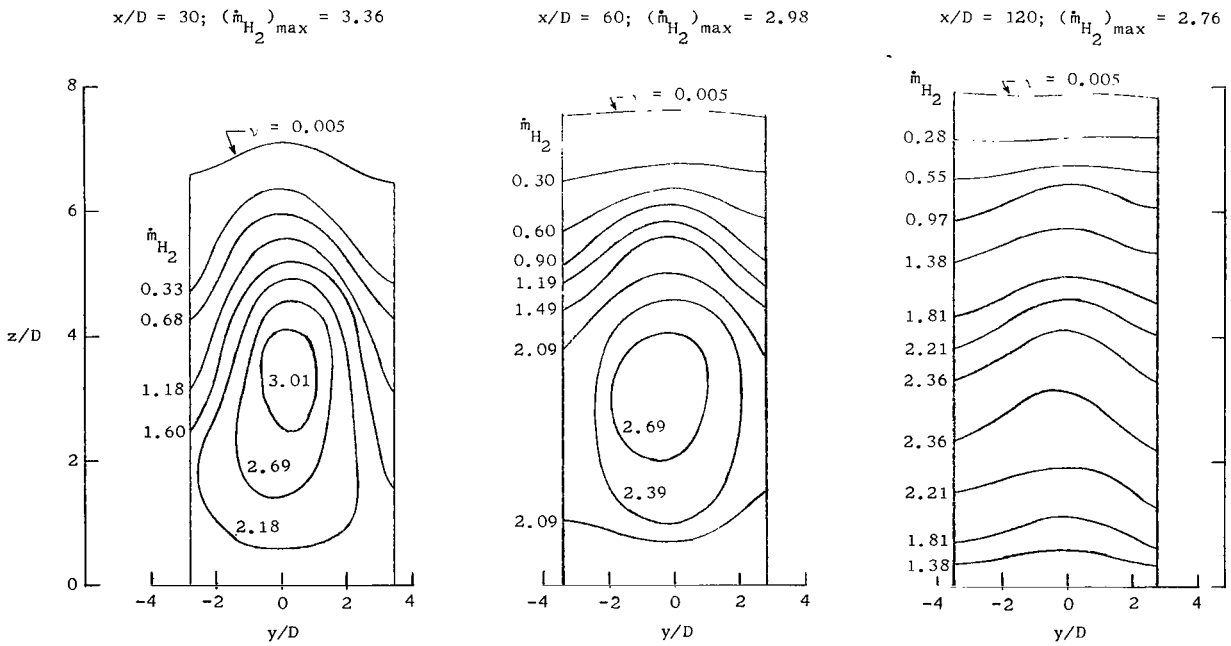

(b) θ = 60°.

Figure 18.- Hydrogen flow rate contours of center jet.

(c) θ = 45°.
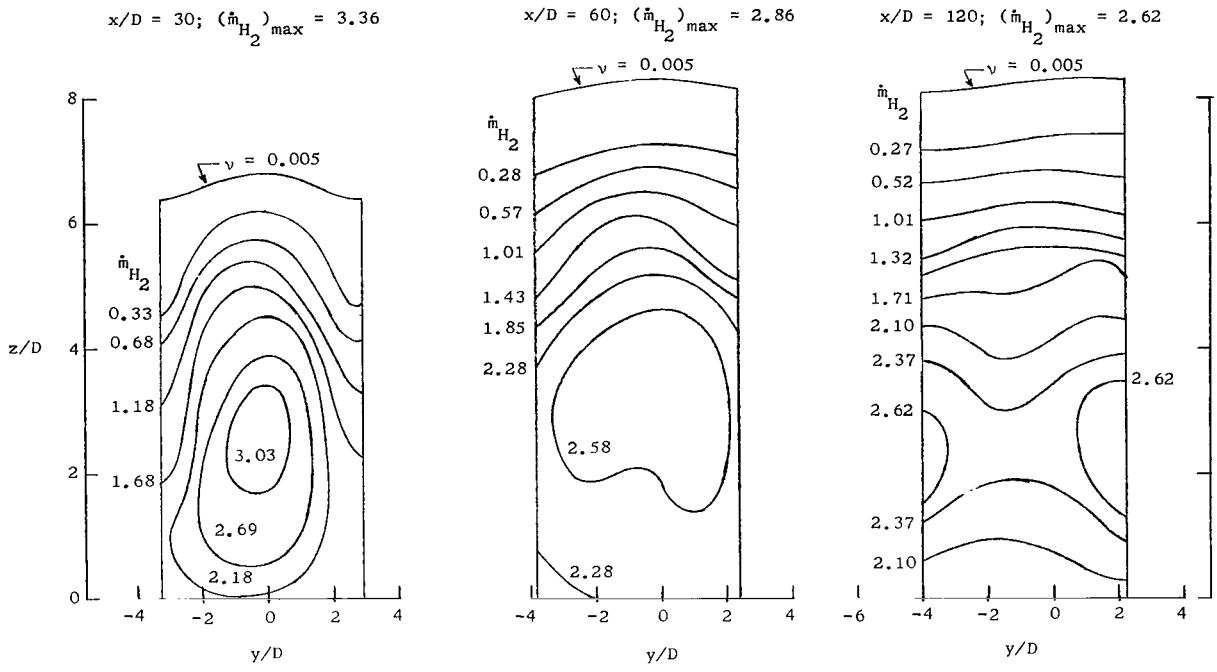
(d) θ = 30°.

Figure 18.- Concluded.

x/D = 30; $(\dot{m}_a)_{max}$ = 261					
●	$\dot{m}_a$	●	$\dot{m}_a$	●	$\dot{m}_a$
1	246	9	94	16	71
2	224	10	62	17	52
3	198	11	56	18	67
4	162	12	52	19	48
5	145	13	67	20	51
6	123	14	47	21	63
7	134	15	49	22	58
8	176				

x/D = 60; $(\dot{m}_a)_{max}$ = 249					
●	$\dot{m}_a$	●	$\dot{m}_a$	●	$\dot{m}_a$
1	216	8	107	15	65
2	155	9	82	16	63
3	133	10	71	17	65
4	101	11	75	18	52
5	90	12	61	19	56
6	96	13	67	20	64
7	128	14	85	21	62

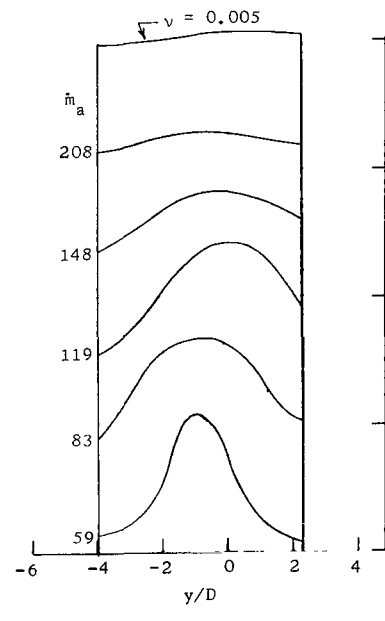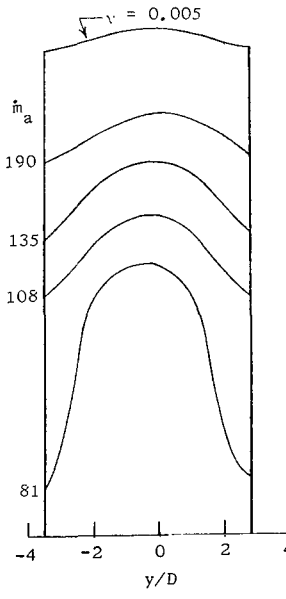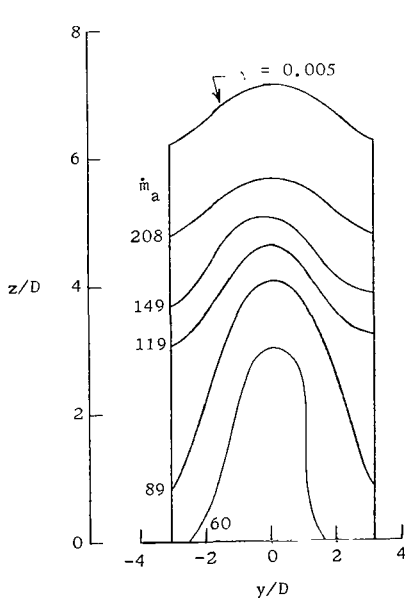| x/D = 120; $(\dot{m}_a)_{max}$ = 283					
●	$\dot{m}_a$	●	$\dot{m}_a$	●	$\dot{m}_a$
1	229	8	129	15	88
2	187	9	112	16	79
3	152	10	98	17	50
4	135	11	84	18	55
5	131	12	71	19	71
6	136	13	76	20	65
7	142	14	87		
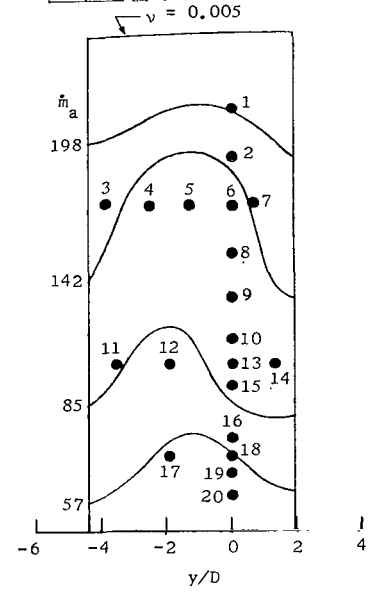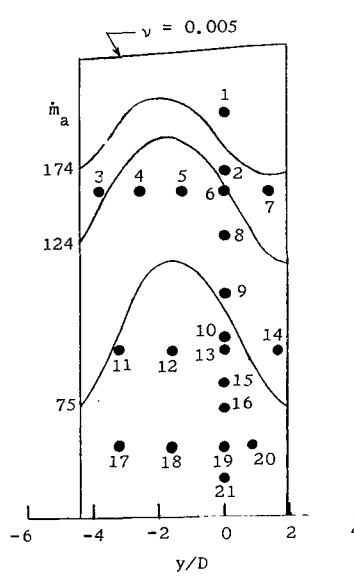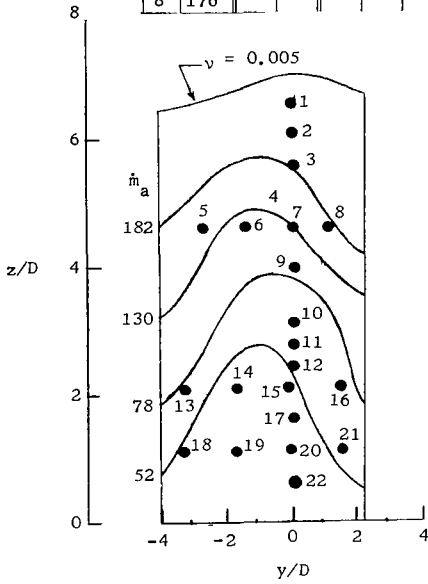
(a)   θ = 90°.

x/D = 30; $(\dot{m}_a)_{max}$ = 298   x/D = 60; $(\dot{m}_a)_{max}$ = 271   x/D = 120; $(\dot{m}_a)_{max}$ = 296

(b)   θ = 60°.

Figure 19.- Air flow rate contours of center jet.

(c) θ = 45°.
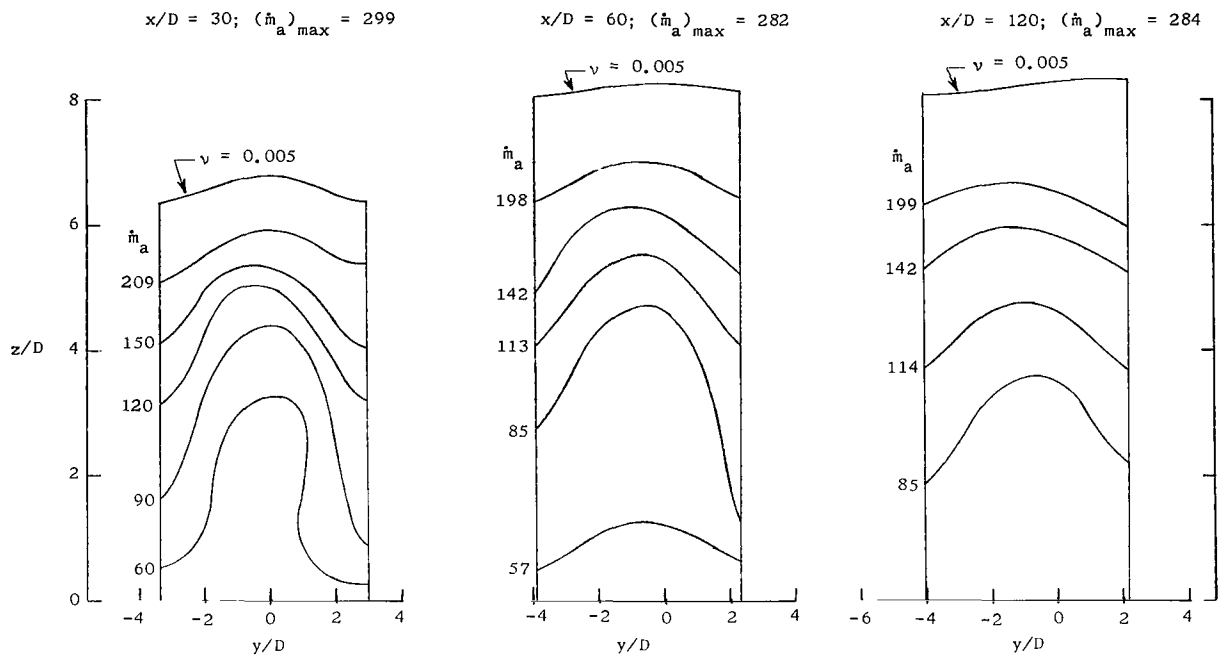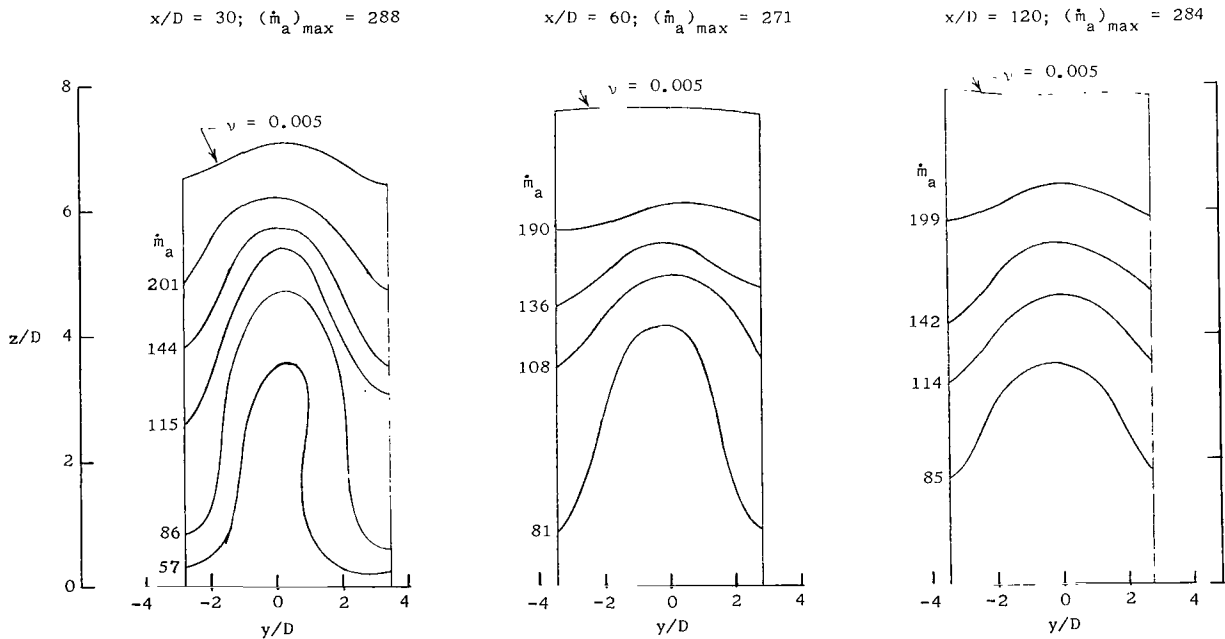
(d) θ = 30°.

Figure 19.- Concluded.

REFERENCES

1. Spaid, F. W.; Zukoski, E. E.; and Rosen, R.: A Study of Secondary Injection of Gases Into a Supersonic Flow. Tech. Rep. No. 32-834, Jet Propulsion Lab., California Inst. Technol., Aug. 1, 1966.

2. Schetz, Joseph A.; Hawkins, Paul F.; and Lehman, Harry: Structure of Highly Under-expanded Transverse Jets in a Supersonic Stream. AIAA J., vol. 5, no. 5, May 1967, pp. 882-884.

3. Billig, F. S.; Orth, R. C.; and Lasky, M.: A Unified Approach to the Problem of Gaseous Jet Penetration Into a Supersonic Stream. AIAA Paper No. 70-93, Jan. 1970.

4. Schetz, Joseph A.; and Billig, Frederick S.: Penetration of Gaseous Jets Injected Into a Supersonic Stream. J. Spacecraft & Rockets, vol. 3, no. 11, Nov. 1966, pp. 1658-1665.

5. Zukoski, Edward E.; and Spaid, Frank W.: Secondary Injection of Gases Into a Supersonic Flow. AIAA J., vol. 2, no. 10, Oct. 1964, pp. 1689-1696.

6. Cohen, Leonard S.; Coulter, Lawrence J.; and Chiappetta, Louis: Hydrocarbon-Fueled Scramjet. Vol. VII — Fuel Distribution Investigation. AFAPL-TR-68-146, Vol. VII, U.S. Air Force, Apr. 1970.

7. Koch, Larry N.; and Collins, Daniel J.: The Effect of Varying Secondary Mach Number and Injection Angle on Secondary Gaseous Injection Into a Supersonic Flow. AIAA Paper No. 70-552, May 1970.

8. Hersch, Martin; Povinelli, Louis A.; and Povinelli, Frederick P.: Optical Study of Sonic and Supersonic Jet Penetration From a Flat Plate Into a Mach 2 Airstream. NASA TN D-5717, 1970.

9. Povinelli, Louis S.; Povinelli, Frederick P.; and Hersch, Martin: A Study of Helium Penetration and Spreading in a Mach 2 Airstream Using a Delta Wing Injector. NASA TN D-5322, 1969.

10. Orth, R. C.; Schetz, J. A.; and Billig, F. S.: The Interaction and Penetration of Gaseous Jets in Supersonic Flow. NASA CR-1386, 1969.

11. Rogers, R. Clayton: A Study of the Mixing of Hydrogen Injected Normal to a Supersonic Airstream. NASA TN D-6114, 1971.

12. Faucher, Joseph E., Jr.; Goldstein, Sidney; and Taback, Edward: Supersonic Combustion of Fuels Other Than Hydrogen for Scramjet Applications. AFAPL-TR-67-12, U.S. Air Force, Feb. 1967.

13. Torrence, Marvin G.: Concentration Measurements of an Injected Gas in a Supersonic Stream. NASA TN D-3860, 1967.

14. Zukoski, Edward E.; and Spaid, Frank W.: Secondary Injection of Gases Into a Supersonic Flow. Jet Propulsion Center, California Inst. Technol., Oct. 1963.

15. Vranos, A.; and Nolan, J. J.: Supersonic Mixing of a Light Gas and Air. Pratt & Whitney Aircraft, United Aircraft Corp., [1964].

16. Torrence, Marvin G.: Effect of Injectant Molecular Weight on Mixing of a Normal Jet in a Mach 4 Airstream. NASA TN D-6061, 1971.

17. Chrans, Larry J.; and Collins, Daniel J.: Stagnation Temperature and Molecular Weight Effects in Jet Interaction. AIAA J., vol. 8, no. 2, Feb. 1970, pp. 287-293.

18. Rogers, R. Clayton: Mixing of Hydrogen Injected From Multiple Injectors Normal to a Supersonic Airstream. NASA TN D-6476, 1971.

19. Pinckney, S. Z.: Static-Temperature Distribution in a Flat-Plate Compressible Turbulent Boundary Layer With Heat Transfer. NASA TN D-4611, 1968.

20. Pinckney, S. Z.: Method for Predicting Compressible Turbulent Boundary Layers in Adverse Pressure Gradients. NASA TM X-2302, 1971.

21. Kaufman, Louis G., II: Hypersonic Flows Past Transverse Jets. Res. Dep. Rep. RE-263 (Contract NOw 65-0396c), Grumman Aircraft Eng. Corp., Aug. 1966. (Available from DDC as AD 637 870.)

22. Eggers, James M.; and Torrence, Marvin G.: An Experimental Investigation of the Mixing of Compressible-Air Jets in a Coaxial Configuration. NASA TN D-5315, 1969.

"The aeronautical and space activities of the United States shall be conducted so as to contribute . . . to the expansion of human knowledge of phenomena in the atmosphere and space. The Administration shall provide for the widest practicable and appropriate dissemination of information concerning its activities and the results thereof."

— NATIONAL AERONAUTICS AND SPACE ACT OF 1958

NASA SCIENTIFIC AND TECHNICAL PUBLICATIONS

TECHNICAL REPORTS: Scientific and technical information considered important, complete, and a lasting contribution to existing knowledge.

TECHNICAL NOTES: Information less broad in scope but nevertheless of importance as a contribution to existing knowledge.

TECHNICAL MEMORANDUMS: Information receiving limited distribution because of preliminary data, security classification, or other reasons.

CONTRACTOR REPORTS: Scientific and technical information generated under a NASA contract or grant and considered an important contribution to existing knowledge.

TECHNICAL TRANSLATIONS: Information published in a foreign language considered to merit NASA distribution in English.

SPECIAL PUBLICATIONS: Information derived from or of value to NASA activities. Publications include conference proceedings, monographs, data compilations, handbooks, sourcebooks, and special bibliographies.

TECHNOLOGY UTILIZATION PUBLICATIONS: Information on technology used by NASA that may be of particular interest in commercial and other non-aerospace applications. Publications include Tech Briefs, Technology Utilization Reports and Technology Surveys.

Details on the availability of these publications may be obtained from:

SCIENTIFIC AND TECHNICAL INFORMATION OFFICE

NATIONAL AERONAUTICS AND SPACE ADMINISTRATION
Washington, D.C. 20546